Syngap1 regulates the synaptic drive and membrane excitability of Parvalbumin-positive interneurons in mouse auditory cortex

Ruggiero Francavilla[1,2], Bidisha Chattopadhyaya[1], Jorelle Linda Damo Kamda[1,2], Vidya Jadhav[1,2], Saïd Kourrich[3,4,5], Jacques L. Michaud[1,2,6], Graziella Di Cristo[1,2,#]

1.CHU Sainte-Justine Azrieli Research Centre, 3175 Côte Ste-Catherine, Montreal, Quebec, Canada H3T 1C5. 2. Department of Neurosciences, Université de Montréal, C.P. 6128, Succ. Centre-Ville, Montreal, Quebec, Canada H3C 3J7. 3. Département des sciences biologiques, UQAM, 141 Av. du Président-Kennedy, Montréal, QC H2X 1Y4, Canada. 4. Centre d'Excellence en Recherche sur les Maladies Orphelines-Fondation Courtois, Pavillon des Sciences biologiques, 141 Avenue du Président-Kennedy, Montréal, QC H2X 3Y7, Canada. 5. Center for Studies in Behavioral Neurobiology, Concordia University, Montreal, QC H4B 1R6, Canada. 6. Department of Pediatrics, Université de Montréal, C.P. 6128, Succ. Centre-Ville, Montreal, Quebec, Canada H3C 3J7.

Corresponding author: graziella.di.cristo@umontreal.ca

Abstract

SYNGAP1 haploinsufficiency-related intellectual disability (SYNGAP1-ID) is characterized by moderate to severe ID, generalized epilepsy, autism spectrum disorder, sensory processing dysfunction and other behavioral abnormalities. While numerous studies have highlighted a role of Syngap1 in cortical excitatory neurons development, recent studies suggest that Syngap1 plays a role in GABAergic inhibitory neuron development as well. However, the molecular pathways by which Syngap1 acts on GABAergic neurons, and whether they are similar or different from the mechanisms underlying its effects in excitatory neurons, is unknown. Here, we examined whether, and how, embryonic-onset *Syngap1* haploinsufficiency restricted to GABAergic interneurons derived from the medial ganglionic eminence (MGE) impacts their synaptic and intrinsic properties in adult primary auditory cortex (A1). We found that *Syngap1* haploinsufficiency significantly affected the intrinsic properties, overall leading to increased firing threshold, and decreased excitatory synaptic drive of Parvalbumin (PV)+ neurons in adult Layer IV A1. Further, the AMPA component of thalamocortical evoked-EPSC was decreased in PV+ cells from mutant mice. Mutant somatostatin (SST)+ interneurons exhibited decreased spontaneous excitatory input and impaired evoked firing without alterations in firing threshold. Finally, we found that the selective blocking of voltage-gated D-type K+ currents was sufficient to rescue PV+ mutant cell-intrinsic properties to wild-type levels. Together, these data suggest that *Syngap1* plays a specific role in the maturation of PV+ cell intrinsic properties and synaptic drive, and its haploinsufficiency may lead to reduced PV cell recruitment in the adult A1, which could in turn contribute to the auditory processing alterations found in SYNGAP1-ID preclinical models and patients.

INTRODUCTION

SYNGAP1 is a key synaptic GTPase-activating protein (GAP) essential for synaptic plasticity, learning, memory, and cognition (Kim et al., 1998; Gamache et al., 2020). Its expression is abundant within forebrain structures, including the cortex and hippocampus (Kim et al., 1998; Porter et al., 2005), where it peaks during critical periods of synaptogenesis (Porter et al., 2005; McMahon et al., 2012; Gou et al., 2020; Jadhav et al, 2024). *SYNGAP1* is increasingly recognised as a candidate gene in neurodevelopmental disorders, with haploinsufficiency leading to intellectual disability (*SYNGAP1*-ID), epilepsy, autism spectrum disorder (ASD), sensory processing deficits, including in the auditory domain, and other behavioral abnormalities (Hamdan et al., 2009; Berryer et al., 2013; Carreño-Muñoz et al., 2022). The role of *Syngap1* has been studied primarily in excitatory neurons. Specifically, *Syngap1* haploinsufficiency has been shown to increase AMPA receptor density and accelerate the maturation of excitatory synapses in hippocampal and somatosensory layer 5 pyramidal cells in rodents (Clement et al., 2012, 2013; Ozkan et al., 2014; Aceti et al, 2015). Similarly, xenotransplantation experiments have shown that SYNGAP1-deficient human cortical neurons transplanted into mouse brains exhibit faster synapse formation and maturation, along with disrupted synaptic plasticity (Vermaercke et al., 2024). In addition to its synaptic roles, *Syngap1* is also implicated in the regulation of cortical neurogenesis of projecting neurons (Birtele et al., 2023).

Although Syngap1 research has predominantly focused on excitatory neurons, its mRNA and protein are also expressed in inhibitory neurons (Zhang et al., 1999; Moon et al., 2008; Berryer et al., 2016; Su et al., 2019; Velmeshev et al., 2019; Zhao and Kwon, 2023; Jadhav et al, 2024). Emerging evidence suggests a role for *Syngap1* in the migration of GABAergic cells and the maturation of inhibitory synapses (Berryer et al., 2016; Su et al., 2019; Sullivan et al., 2020; Khlaifia et al., 2023); nevertheless, whether the underlying cellular and molecular mechanisms are similar to those observed in excitatory cells is unknown.

Cortical inhibitory neurons can be broadly classified into two major subtypes based on their anatomy, physiology and expression of specific markers: parvalbumin- (PV+) and somatostatin- (SST+) expressing interneurons (Rudy et al., 2011). These subtypes provide perisomatic and distal dendritic inhibition to pyramidal cells, respectively (Levy and Reyes, 2012; Yavorska and Wehr, 2016). Due to the specificity in their synapse location and distinct functional properties, SST+ and PV+ neurons differentially shape excitatory neuronal responses. By providing fast inhibition onto postsynaptic pyramidal cell somata and proximal dendrites, PV+ cells exert fine control on their output (Moore and Wehr, 2013; Tremblay et al., 2016), while SST+ cells targeting apical dendrites of postsynaptic pyramidal cells exert specific control over dendritic synaptic integration (Kawaguchi and Kubota, 1997; Chiu et al., 2013). We recently showed that prenatal-onset *Syngap1* haploinsufficiency restricted to Nkx2.1-expressing GABAergic interneuron precursors, which include PV+ and SST+ interneurons, leads to the development of alterations in auditory cortex activity (Jadhav et al., 2024), which resemble those observed in global *Syngap1* haploinsufficient mouse models and *SYNGAP1*-ID patients (Carreño-Muñoz et al., 2022), suggesting that interneuron dysfunction may contributes to these specific phenotypes. However, how prenatal-onset *Syngap1* haploinsufficiency in GABAergic interneurons alters their physiology in adult cortex is unknown.

To address this question, we generated conditional transgenic mice wherein *Syngap1* haploinsufficiency was restricted to MGE-derived interneurons. We then assessed the synaptic and intrinsic properties of PV+ fast spiking (FS) and SST+ regular spiking cells in layer IV of the adult primary auditory cortex (A1). We found that both mutant PV+ and SST+ cells show decreased excitatory synaptic drive. Notably, PV+, but not SST+, interneurons showed a significantly increased threshold for action potential (AP) generation, pointing towards a reduced recruitment of cortical PV cells in the mutant mouse. Further, we were able to partially restore PV+ cell function *ex vivo* using alpha-dendrotoxin (α-DTX), a selective blocker of Kv1 family voltage-gated D-type

K+ currents. Overall, these results suggest that Syngap1 can affect neuronal physiological properties by modulating distinct molecular mechanisms in a cell type-specific manner.

RESULTS

Syngap1 haploinsufficiency in MGE-derived interneurons is associated with decreased synaptic excitation in PV+ cells

Since Syngap1 has been shown to regulate AMPAR-mediated synaptic transmission in hippocampal and cortical excitatory neurons and hippocampal inhibitory neurons (Ozkan et al., 2014; Arora et al., 2022; Khlaifia et al., 2023), we first explored whether embryonic-onset *Syngap1* haploinsufficiency in MGE-derived cortical interneurons affects their glutamatergic synaptic inputs in adult A1. We performed targeted voltage-clamp recordings of spontaneous (sEPSCs) and miniature excitatory postsynaptic currents (mEPSCs) in layer IV (LIV) EGFP-expressing interneurons from auditory thalamocortical slices of 9-13 weeks-old Tg(*Nkx2.1-Cre*):$RCE^{f/f}$:$Syngap1^{+/+}$ (control) and Tg(*Nkx2.1-Cre*):$RCE^{f/f}$:$Syngap1^{f/+}$ (cHet) littermates (***Figure 1, Table 1***). Nkx2.1-expressing MGE precursors generate most of PV+ and SST+ cortical interneurons (Xu et al., 2008), while the RCE allele drive Cre-dependent EGFP expression. Recorded MGE-derived interneurons were filled with biocytin, and their identity was confirmed by immunolabeling for neurochemical markers (PV or SST) and analysis of anatomical properties, including location of the axonal arborisation across different cortical layers and presence or absence of dendritic spines (***Figure 1a, Suppl. Figure 1***) (Kawaguchi and Kubota, 2006; Rock et al., 2018; Bertero et al., 2020). All results were analysed by linear mixed model (LMM), modelling animal as a random effect and genotype as the fixed effect. This method was chosen for statistical analysis because it accounts for both animals as independent replicates and cell recorded in each mouse as repeated/correlated measures, thus providing the most accurate approach for assessing the data (Aarts et al., 2014; Yu et al 2022).

We found that sEPSC amplitude was decreased in LIV PV+ neurons from cHet mice compared to those recorded in control littermates (***Figure 1c right***). sEPSC rise and decay time constants were not significantly different between the two genotypes (***Table 1***), suggesting that postsynaptic AMPA receptor subunit composition was not affected by *Syngap1* haploinsufficiency. To discern whether *Syngap1* haploinsufficiency had a pre or postsynaptic effect on the glutamatergic drive received by PV+ cells, we analysed mEPSC recorded from the same neurons shown in Figure 1b-e (***Figure 1f-j***). We confirmed that TTX blocked APs in PV+ cells and that recordings were stable as indicated by lack of changes in series resistance during the recording period in our experimental setup (***Suppl. Figure 2f-i)***. We found no difference in mEPSC amplitude between the two genotypes (***Fig. 1g, right***), indicating that the observed difference in sEPSC amplitude (***Figure 1c, right***) could be due to impaired AP-dependent release in cHet mice and the presence of large-amplitude sEPSCs that are preferentially affected by TTX in control mice (***Suppl. Figure 2b-e***). Conversely, cHet mice showed longer inter-mEPSC time interval (***Figure 1g, left***, for inter-cell mean comparison LMM, p=0.056, for cumulative distributions LMM, p=0.045**)**, and significantly lower charge transfer and ΔQ*f (***Figure 1j***) compared to controls littermates, suggesting a decrease of glutamatergic presynaptic release sites onto PV+ cells. Recent studies, based on serial block-face scanning electron microscopy, suggest that cortical PV+ interneurons receive more robust excitatory inputs to their perisomatic region than pyramidal neurons (Hwang et al., 2021; Elabbady et al., 2025). Quantification of the density of putative glutamatergic synapses onto PV+ cell somata, identified by the colocalization of the vesicular glutamate 1 (vGlut1, presynaptic marker) and PSD95 (postsynaptic marker), revealed a significant decrease in cHet compared to control mice (***Suppl. Figure 3a,b***). Whether the density of dendritic targeting excitatory inputs is affected as well remains an open question.

In A1, layer IV PV+ cells receive stronger subcortical thalamocortical inputs compared to excitatory cells and other subpopulations of GABAergic interneurons (Ji et al., 2016; Rock et al., 2018). We thus recorded evoked AMPA (eAMPA)- and NMDA (eNMDA)-mediated currents in PV+ cells by bulk electrical stimulation of the thalamic radiation (***Figure 2a-f, Table 2***), to determine whether thalamocortical synapses were affected by conditional *Syngap1* haploinsufficiency. eAMPA amplitude, area under the curve (AUC) charge transfer (average of all responses, successes + failures, ***Figure 2b right,c***) and potency (average of all successes only, ***Figure 2e left***) were decreased in cHet mice as compared to control littermates. In addition, we found a substantial increase in onset latencies of eAMPA currents (***Figure 2d***), suggesting a potential deficit in the thalamocortical recruitment of PV+ cells. Next, we assessed eNMDA currents in PV+ cells in presence of $GABA_AR$, $GABA_B$ and AMPA inhibitors (1 μM Gabazine, 2 μM CGP, and 10 μm NBQX, respectively) (***Figure 2c,e***). We found that eNMDA currents as well as the fraction of PV+ cells showing these responses were similar in cHet and control littermates (***Figure 2c right, 2e left***), therefore leading to increased NMDA/AMPA in cHet mice (***Figure 2e right***). Interestingly, the kinetics of eAMPA and eNMDA currents were similar in both genotypes, indicating no change in their subunit composition (***Figure 2f, Table 2***). These results suggest that embryonic-onset *Syngap1* haploinsufficiency in MGE-derived interneurons specifically impairs AMPA-mediated thalamocortical recruitment of PV+ cells. Of note, the density of putative thalamocortical glutamatergic synapses onto PV+ cell somata, identified by the colocalization of the vesicular glutamate 2 (vGlut2, thalamocortical presynaptic marker) and PSD95 (postsynaptic marker) was not significantly different in cHet as compared to littermate controls (***Suppl. Figure 3c,d***), suggesting that presynaptic release from excitatory thalamocortical fibers or/and AMPARs expression at thalamocortical synapses on PV+ cells are likely decreased in cHet mice.

To further explore this phenomenon, we performed paired pulse ratio (PPR) experiments, as PPR typically reflects changes in presynaptic release probability (***Figure 2g,h***). We found that, in contrast with Control mice, evoked excitatory inputs to layer IV PV+ cells showed paired-pulse

facilitation in cHet mice (***Figure 2g,h***), suggesting that thalamocortical presynaptic sites likely have decreased release probability in mutant compared to control mice.

Since PV+ cell recruitment is regulated by the balance of its excitatory and inhibitory inputs, we next analysed spontaneous (sIPSCs) and miniature inhibitory postsynaptic currents (mIPSCs) recorded from layer IV PV+ cells in both genotypes. We observed reduced sIPSC amplitude in cHet compared to control PV+ cells (***Figure 3a,b, Table 3***); however, mIPSC analysis revealed no genotype-dependent differences in any parameters (***Figure 3f-j, Table 3***), suggesting that decreased sIPSC amplitude in cHet PV+ cells was likely due to changes in presynaptic cell-intrinsic excitability and/or network activity.

cHet mice show decreased layer IV PV+ cell-intrinsic excitability

PV+ cell recruitment in cortical circuits is dependent on both their synaptic drive and intrinsic excitability. Thus, we sought to investigate how *Syngap1* haploinsufficiency in MGE-derived interneurons impacts the intrinsic excitability and firing properties of PV+ cells, by performing whole-cell current-clamp recordings (***Figure 4, Table 4***). We found no changes in passive membrane properties (Cm, Rin and τ) of PV+ cells recorded from cHet mice as compared to control littermates (***Figure 4a***); conversely, analysis of active membrane properties revealed a significant decrease in the excitability of mutant PV+ cells (***Figure 4b,c***). In particular, cHet PV+ cells showed reduced AP amplitude, and increased AP threshold and latency to first AP (***Figure 4b,c***, ***Table 4***). In line with the decrease in intrinsic excitability, the threshold current was increased in PV+ cells from cHet mice (***Figure 4d***). Both cHet and control PV+ cells displayed typical, sustained high-frequency trains of brief APs with little spike frequency adaptation in response to incremental current injections (***Fig. 4e, right***); however, cHet PV+ interneurons fired significantly fewer APs in response to the same depolarizing current injection when compared to control mice (***Figure 4e, left***; Two-way Repeated Measure ANOVA with Sidak's multiple comparison post hoc test,

****p<0.0001). These data show that embryonic-onset *Syngap1* haploinsufficiency in PV+ cells impair their basic intrinsic and firing properties.

Embryonic-onset *Syngap1* haploinsufficiency in MGE-derived interneurons differentially impacts dendritic arborization and intrinsic properties of distinct PV+ cell subpopulations

The majority of PV+ cells are classified as FS cells, due to their ability to sustain high-frequency discharges of APs (***Figure 4e, right***). However, clusters of atypical PV+ cells have been previously reported in several brain regions including subiculum (Nassar et al., 2015), striatum (Bengtsson Gonzales et al., 2020), hippocampus (Ekins et al., 2020) and somatosensory cortex (Helm et al., 2013). While atypical PV+ cells share many electrophysiological parameters with FS cells, they have a slower AP half-width and possess a lower maximal AP firing frequency (Helm et al., 2013; Nassar et al., 2015; Bengtsson Gonzales et al., 2018; Ekins et al., 2020;). Using these 2 criteria, we found a moderate negative correlation between F_{max}initial and AP half-width in both genotypes (***Figure 5a, left***). This suggests that PV+ cell with broader AP durations may have a lower F_{max}initial, a feature previously observed in atypical PV+ cells from other cortical areas (Helm et al., 2013; Nassar et al., 2015; Bengtsson Gonzales et al., 2018; Ekins et al., 2020). To further investigate whether A1 PV+ cells from control mice could be functionally segregated into distinct clusters, we performed hierarchical clustering of AP half-width and F_{max}initial values based on Euclidean distance (***Figure 5a, right***). This analysis identified two clusters of PV+ cells: one with short AP half-widths associated with higher F_{max}initial values, and another with broader AP durations and lower F_{max}initial values, consistent with what reported in other cortical regions (Helm et al., 2013; Nassar et al., 2015; Bengtsson Gonzales et al., 2018; Ekins et al., 2020). Although hierarchical clustering distinguished these two subgroups, a few PV+ cells with longer AP half-widths exhibited F_{max}initial values typical of PV+ cells with shorter AP half-widths (***Figure 5a, right***), indicating that these two parameters alone may not be sufficient to fully differentiate subtypes within our PV+ cell dataset. We thus decided to perform PCA analysis using additional

key intrinsic physiological features such as passive (V_m, R_{in}, C_m) and active (threshold current, AP half-width, AP amplitude, first AP latency, AP threshold, fAHP amplitude, amplitude AR, frequency AR, F_{max}initial and F_{ss}) membrane properties (***Figure 5b, left***). We then selected the intersection point of the two AP half-width distributions in control and cHet mice as a cut-off to define two different subpopulations of PV+ cells: Basket Cell (BC)-short (AP half-width <0.78ms) and BC-broad (AP half-width ≥0.78ms) (***Figure 5c,d***). In control mice, these two PV+ cell subtypes showed major differences in R_{in}, C_m, F_{max}initial and F_{ss} (***Table S1***, comparison between BC-short and BC-broad in control mice). PCA analysis also revealed that, while two distinct PV+ cell subgroups were clearly distinguishable in control mice, these differences were more ambiguous in cHet mice, wherein some BC-short cells fell within the BC-broad subgroup (***Figure 5d***). In addition, we observed that the fraction of BC-short cells was increased in cHet compared to control mice (61% vs 41% of total PV+ cells, respectively), suggesting that *Syngap1* haploinsufficiency affects specific subgroups of PV+ cells (***Figure 5d***).

Next, we examined whether the diversity in PV+ cell electrophysiological profiles was reflected in their dendritic arborisation (***Figure 5e-h, Table 5.1- 5.4***). We also measured the anatomical location of cell bodies (distance in µm from the pia) to confirm that the recorded and analyzed cells were situated within LIV (***Figure 5g,h***). In control mice, both BC-short and BC-broad cells showed ovoid somata and multipolar dendrites (***Figure 5e,f***). Anatomical reconstruction and morphometric analysis revealed differences in dendritic arborization that correlated positively with AP half-width in control mice (***Figure 5g,k***). In particular, BC-short cells showed significantly lower branch point numbers and dendritic surface area as compared to BC-broad cells (***Figure 5g***). In contrast, the dendritic arbor of BC-short neurons vs BC-broad did not show significant differences in cHet mice (***Figure 5h***). Direct comparison of PV+ cell dendritic arbor in cHet vs control littermates clearly showed that BC-short neurons were specifically affected by *Syngap1* haploinsufficiency (***Figure 5i, j***), with BC-short cells from cHet mice showing a significant increase in dendritic complexity

compared to those from control mice (***Figure 5i***). Further, the strong positive correlation of dendritic surface area with AP half-width was present only in PV+ cells from control mice but disappeared in cHet mice (***Figure 5k***). Altogether, these data indicate that embryonic-onset *Syngap1* haploinsufficiency in Nkx2.1+ interneurons alters dendritic development in a specific subpopulation of PV+ cells, leading to the increased dendritic area and complexity. These structural changes may, in turn, affect their intrinsic excitability and the dendritic integration of synaptic inputs.

Based on the observed heterogeneity in morpho-electric parameters of PV+ cells, we next sought to investigate the effect of *Syngap1* haploinsufficiency on the intrinsic excitability of specific PV+ cell subtypes (***Figure 6, Tables 6.1, 6.2***). We found that BC-short cells showed preserved passive membrane properties (***Figure 6a***) but altered active membrane properties (***Figure 6b-e***) in cHet compared to control mice. In particular, we found increased AP threshold affecting AP amplitude (***Figure 6b,c***) and increased threshold current (***Figure 6d***), indicating a decrease in the excitability of cHet BC-short cells. cHet BC-short interneurons displayed AP firing patterns similar to those in control BC-short (***Figure 6e, right***), but fired less APs in response to somatic depolarization (***Figure 6e, left***, Two-way Repeated Measure ANOVA with Sidak's multiple comparison post hoc test, ****$p<0.0001$). In contrast, BC-broad neurons had a more hyperpolarized RMP (***Figure 6f***), and increased AP latency and threshold (***Figure 6g,h***) in cHet mice compared to controls. However, in cHet BC-broad neurons these changes were not translated into decreased ability to generate spikes (***Figure 6i,j***, Two-way Repeated Measure ANOVA with Sidak's multiple comparison post hoc test, $p= 0.333$). Altogether these data suggest that BC-short neurons may be overall more vulnerable to *Syngap1* haploinsufficiency than BC-broad neurons. They further indicate that *Syngap1* levels appears to play a common role in determining the threshold for AP generation in all adult PV+ cells.

***Syngap1* haploinsufficiency in MGE-derived interneurons affects SST+ interneurons firing and spontaneous excitatory inputs**

To investigate whether the observed alterations in the synaptic and intrinsic properties of PV+ interneurons are cell-type-specific, we next examined whether the second major group of Nkx2.1-expressing cortical interneurons, the SST+ interneurons, exhibits similar changes. In current-clamp recordings, control SST+ cells displayed a low firing rate and characteristic AP frequency accommodation in response to incremental current injections (***Figure 7a, Table 7***). Morphologically, SST neurons showed ovoid-shaped somata, multipolar (***Suppl. Figure 1b, left***) or bitufted (***Suppl. Figure 1b, right***) dendritic arbours with spines. Their axon projected into layer I, where it arborized giving rise to multiple collaterals. The molecular identity of this interneuron subtype was confirmed by immunopositivity for SST+ and immunonegativity for PV (***Figure 7b, Suppl. Figure 1b***). Interestingly, PCA analysis using the previously mentioned electrophysiological parameters clearly distinguished SST+ neurons from BC-short subtype of PV+ cells, but showed an overlap between BC-broad PV+ and SST+ cells (***Figure 7c***). These data indicate that, in mature A1, a subtype of PV+ cells share some electrophysiological features with SST+ cells, indicating the necessity to perform post-hoc immunohistochemical validation (***Figure 7b,c***). cHet SST+ cells showed no significant changes in the active or passive membrane properties we analysed (***Figure 7d,e***). However, their evoked firing properties were affected, with fewer APs in response to the same depolarizing current injection compared to control SST+ cells (***Figure 7f***, Two-way Repeated Measure ANOVA with Sidak's multiple comparison post hoc test, ***$p<0.001$). Furthermore, we found that sEPSC amplitude and charge transfer were significantly decreased in SST+ neurons from cHet mice compared to control littermates (***Suppl. Figure 4; Table S2***).

Thus, embryonic-onset *Syngap1* haploinsufficiency in MGE-derived interneurons significantly reduced spontaneous excitatory inputs and evoked firing properties of both PV+ and SST+.

However, alterations in AP initiation, as indicated by an increased firing were observed exclusively in PV+ cells (***Figure 6c,h***), suggesting a selective impairment in their intrinsic excitability.

A selective Kv1-blocker rescues PV+ cell intrinsic excitability in cHet mice

Based on previous studies performed in PV+ cells (Wang et al., 1994; Goldberg et al., 2008; Zurita et al., 2018), changes in voltage-gated D-type K+ currents mediated by the Kv1 subfamily could account for the observed altered AP threshold observed in cHet mice. To test this hypothesis, we performed current-clamp recordings from PV+ cells in control and cHet mice in presence or absence of α-DTX (100 nM), a specific blocker of channels containing Kv1.1, Kv1.2 or Kv1.6 (***Figure 8a-e, Table 8***). As hypothesized, the presence of α-DTX rescued the voltage threshold for AP generation in cHet PV+ cells to control levels, without affecting the AP shape (***Figure 8 a,b,c, Table 8***), while the relation between the AP number and current injection remained the same (***Figure 8d***), indicating that α-DTX had no impact on PV+ cell firing. Further, α-DTX facilitated AP initiation in cHet PV+ cells by reducing AP delay from stimulation onset (***Figure 8e***). These data suggest that *Syngap1* haploinsufficiency may enhance voltage-gated D-type K+ currents, thereby leading to reduced excitability of PV+ cells in the adult A1.

DISCUSSION

In this study, we investigated the impact of embryonic-onset, MGE-restricted *Syngap1* haploinsufficiency on the intrinsic and synaptic properties of the two major cortical GABAergic interneuron subtypes, PV+ and SST+ cells. In particular, mutant PV+ cells showed reduced intracortical and thalamo-cortical glutamatergic synaptic drive. We further found that *Syngap1* haploinsufficiency has a significant impact on the intrinsic properties, in particular AP threshold, of PV+ cells, resulting in overall decreased excitability. The intrinsic excitability of PV+ cells was rescued in part by pharmacological inhibition of voltage-gated D-type K+ current mediated by the

Kv1 subfamily, suggesting that this current may serve as molecular mediator of the functional deficits induced by *Syngap1* haploinsufficiency. *Syngap1* has been studied mainly in the context of synaptic physiology; therefore, our data highlights a novel aspect of *Syngap1* biology.

Since *Syngap1* mRNA expression in PV+ and SST+ cells is not limited to A1 (Zhao and Kwon, 2023; Jadhav et al, 2024), it is likely that its haploinsufficiency may affect interneurons physiology in other cortical regions, as well. In our mouse model, Syngap1 haploinsufficiency is driven by the expression of Nkx2.1, which has an embryonic onset (E10.5). However, *Syngap1* expression is thought to be highest during critical periods of synaptogenesis (Porter et al., 2005; McMahon et al., 2012; Gou et al., 2020; Jadhav et al, 2024). Therefore, the precise developmental time window during which *Syngap1* insufficiency disrupts PV+ neuron properties, remains to be determined.

Syngap1 is thought to be a potent regulator of excitatory synapses and its reduced expression in excitatory cells causes an increase in AMPA receptor density and premature maturation of excitatory synapses (Rumbaugh et al., 2006; Clement et al., 2012; 2013). Unexpectedly, here we found that *Syngap1* haploinsufficiency restricted to MGE-derived interneurons depresses glutamatergic synaptic transmission, potentially via presynaptic mechanisms. In addition, LIV PV+ cells receive the strongest thalamocortical input compared to excitatory cells and other subpopulation of GABAergic interneurons (Ji et al., 2016; Zuritasc et al., 2018). Our study indicates that a reduction in AMPA-mediated thalamocortical transmission onto LIV PV+ cells may contribute to the deficit in glutamatergic drive, as suggested by facilitated PPR in cHet compared to control mice. This, combined with the increased onset latencies of thalamocortical-evoked AMPA responses along with an enhanced NMDA/AMPA ratio, points to both a likely decrease in presynaptic release from thalamocortical fibers and impaired recruitment of PV+ cells by thalamic inputs in cHet mice.

How could *Syngap1* haploinsufficiency in Nkx2.1-expressing cells affect the glutamatergic drive coming from local and thalamic excitatory cells? Our data suggest a role of Syngap1 in promoting

GABAergic cell intrinsic excitability during normal development. These findings are in line with recent data reporting a decrease in intrinsic excitability of developing cortical excitatory cells in *Syngap1*$^{+/-}$ mice (Arora et al., 2022). In PV+ cells, connectivity and cell excitability are reciprocally regulated at the circuit level (Favuzzi et al., 2017); thus, it is possible that early-onset *Syngap1* haploinsufficiency in MGE-derived interneurons may first affect the development of their intrinsic excitability properties, which in turn would modulate the maturation of their excitatory drive, and activity levels in adulthood. Alternatively, homeostatic adaptation of PV+ interneurons in response to the decreased number of excitatory inputs could trigger changes in voltage-gated D-type K+ currents (Dehorter et al., 2015; Favuzzi et al., 2017). Therefore, Syngap1 may play complex roles at the cellular level and at different developmental stages, based on the crosstalk between neuronal activity levels and Syngap1 localisation and interaction with other proteins. The use of a conditional genetic strategy to induce *Syngap1* haploinsufficiency specifically in MGE-derived interneurons allow investigating its effects in these GABAergic populations; however, it is important to highlight the limit of this approach, since whether GABAergic interneurons physiology would be similarly affected within an entire network carrying the same mutation (thus affecting also excitatory neurons) remains to be established.

Based on morphology and synaptic targets, three main subgroups of PV+ cells have been identified in auditory cortex, ie basket cells (BCs), chandelier cells and long-range projecting PV+ cells (Levy and Reyes, 2012, Rock et al., 2018; Zurita et al., 2018; Bertero et al., 2019). Despite differences in morphology and target selectivity, different PV+ cell subgroups share common electrophysiological features such as short AP-half width, low input resistance, very high threshold current, and relatively small AP amplitude. In particular, while clusters of atypical BC PV+ have been previously reported in several areas (Helm et al., 2013; Nassar et al., 2015; Bengtsson Gonzales et al., 2018; Ekins et al., 2020), auditory cortex PV+ BCs have been considered as a homogeneous electrophysiological group (Studer and Barkat, 2022). One of the key findings of this study is that

mature A1 contains at least two distinct morphological and electrophysiological subgroups of PV+ BCs, including a subgroup with an unexpectedly broader AP half-width (Table S1). The genetic tools used to identify PV+ cells (*PV_Cre* or G42 mice vs *Nkx2.1*_Cre mice) might selectively label a specific PV+ BC cell subtype. Alternatively, the distribution of different PV+ BC subtypes could depend on the cortical region and layer. The presence of at least two PV+ BC subtypes with different electrophysiological characteristics may partly explain the previously observed variability in the recruitment of auditory cortex PV+ cells in vivo (Seybold et al., 2015; Phillips and Hasenstaub, 2016; Keller et al., 2018; Gothner et al., 2021), as these differences could arise from the AP half-width criteria used to sort FS cells.

Despite the differences observed in how *Syngap1* haploinsufficiency affects the anatomy and physiological properties of the two PV+ cell subtypes, a shared deficit we observed was the decrease in intrinsic excitability, as suggested by the increased AP threshold affecting AP initiation. In PV+ cells, voltage-gated D-type K+ currents mediated by the Kv1 family strongly contribute to AP generation, making them effective targets for modifying AP latency, threshold and rheobase current in these cells (Wang et al., 1994; Goldberg et al., 2008; Zurita et al., 2018). Here, we indeed restored the excitability of mutant PV+ cells by pharmacologically inhibiting this channel family using α-DTX; however, whether Kv1 currents or/and channel density are altered in mutant PV+ cells remain to be investigated. Consistent with our findings, Arora et al. (2022) rescued pyramidal cell intrinsic excitability and neuronal morphology via lowering elevated potassium channels, by expressing a dominant negative form of the Kv4.2 potassium channel subunit, dnKv4.2, in developing *Syngap1* mutant mice. Kv4.2 and Kv1 potassium channels modulate the intrinsic excitability of pyramidal cell and PV+ interneurons, respectively, indicating that the action of Syngap1 on potassium channels may be a general mechanism. A recent study focusing on the PSD interactomes of Syngap1 isolated from adult homogenized mouse cortex suggested a physical interaction between Syngap1 and the potassium channel auxiliary subunit Kvβ2 (Wilkinson et al.,

2017). Since Kvβ2 regulates the translocation of Kv1 channels in dopaminergic neurons and potentially PV+ cells (Okaty et al., 2009; Yee et al., 2022), it is possible that *Syngap1* haploinsufficiency may lead to dysregulated Kv1 translocation at the membrane, leading to excessive K currents. Of note, both Kv1 channels and Syngap1 are developmentally regulated (Okaty et al., 2009; Gamache et al., 2020), thus *Syngap1* hypofunction may lead to dysregulation of genes encoding voltage-gated potassium channel affecting cell maturation and excitability.

Interestingly, the alterations in intrinsic excitability were less pronounced in cHet SST+ interneurons, primarily affecting their firing rate. This discrepancy could be due to the heterogeneity of SST+ interneurons likely present in our dataset (Scala et al., 2019; Hostetler et al., 2023). In addition, it's possible that other intrinsic factors, not assessed in this study, may have contributed to this effect. For example, in SST+ cells the differences in the AHP kinetics depend predominantly on the presence of a second slower AHP component impacting the overall amplitude, slope and duration of the AHP (Riedemann et al., 2018). Recent studies also showed that SYNGAP1 interacts with Kv4 (Wilkinson et al., 2017). Since somato-dendritic Kv4 channels in SST+ interneurons contribute to the regulation of their firing (Serôdio and Rudy, 1998; Bourdeau et al., 2007), *Syngap1* haploinsufficiency could affect SST+ cell excitability via this channel.

PV+ cells have a fundamental role in generating and maintaining gamma oscillations in the brain (Cardin et al., 2009). In particular, recent studies have also shown that deficiency in PV interneuron-mediated inhibition contribute to increased baseline cortical gamma rhythm (Spencer, 2012; Carlén et al., 2012), a phenotype we observed in the auditory cortex of germline *Syngap1*$^{+/-}$ mutant mice, *SYNGAP1*-ID patients (Carreño-Muñoz et al., 2022) and mice with conditional *Syngap1* haploinsifficiency restricted to MGE-derived interneurons (Jadhav et al., 2024). Specifically, PV+ interneurons, which target the perisomatic domain of pyramidal neurons, are adapted for fast synchronization of network activity controlling spike timing of the excitatory network in auditory cortex (Wehr and Zador, 2003; Li et al. 2014). To sharpen the tuning of

neighboring pyramidal cells, PV+ interneurons need to be more effectively recruited by excitatory inputs so that they can restrict the temporal summation of excitatory responses of their pyramidal cell targets and increase the temporal precision of their firing (Povysheva et al., 2006). Our study suggests that decrease in AMPA-mediated thalamocortical input onto LIV PV+ cells along with deficits in their intrinsic excitability could account for altered spike timing of pyramidal cells causing an increase in overall network excitability.

An open question remains whether synaptic properties differ among PV+ cell subtypes, which we could not address due to technical limitations. These include the lack of specific neurochemical markers to distinguish between the two PV+ subtypes (Ekins et al., 2020), and the use of a Cs+-based internal solution required for voltage-clamp experiments, which prevents the recording of neuronal firing. It could be interesting to correlate PV expression levels directly with AP half-width, since BC-short may express higher levels of PV compared to BC-broad as already found in the striatum using patch seq approach (Bengtsson Gonzales et al., 2020). Further, in our studies, we used a conditional mouse model where *Syngap1* haploinsufficiency is restricted to specific cell types, namely MGE-derived interneurons. Since cell-type specific genetic mutations do not typically occur in humans, it would be interesting to investigate whether *SYNGAP1*-haploinsufficient human-derived neurons show alterations in specific GABAergic subpopulations-intrinsic and synaptic properties. Further, whether and how PV+ physiology is affected in global haploinsufficient mice remain to be addressed. Of note, global haploinsufficient *Syngap1* mice, *SYNGAP1*-ID patients and MGE-restricted *Syngap1* haploinsufficient mice show comparable abnormal phenotypes in cortical auditory processing (Carreño-Muñoz et al., 2022; Jadhav et al., 2024). Further experiments specifically targeting PV+ cell activity, using targeted chemogenetic or pharmacological approach (Kourdougli et al., 2023) are required to shed light on the role PV+ interneuron hypoactivity in these phenotypes.

MATERIALS AND METHODS

Mice

All procedures and experiments were done in accordance with the Comité Institutionnel de Bonnes Pratiques Animales en Recherche (CIBPAR) of the CHU Ste-Justine Research Center in line with the principles published in the Canadian Council on Animal's Care's. Mice were housed (2-5 per cage), maintained in a 12/12 h light/dark cycle, and given ad libitum access to food and water. Experiments were performed in 9-13 weeks-old male mice during the light phase. To investigate the effects of *Syngap1* haploinsufficiency in cortical PV+ and SST+ interneurons, we generated mice heterozygous for the *Syngap1* conditional allele (*Syngap1*$^{f/f}$; Jackson Laboratories; #029303) under the Tg(*Nkx2.1-Cre*) driver line (Jackson Laboratories; #008661) and further crossed them with mice carrying the RCE allele (Jackson Laboratories; #032037) to generate Tg(*Nkx2.1-Cre*):*RCE*$^{f/f}$:*Syngap1*$^{+/+}$ and Tg(*Nkx2.1-Cre*):*RCE*$^{f/f}$:*Syngap1*$^{f/+}$ mice, for targeted recordings. Nkx2.1-expressing cells were identified by the expression of EGFP, since the RCE allele allow Cre-dependent EGFP expression.

Acute slice preparation

Briefly, animals (age range, mean ± S.E.M.: 75.5 ± 1.8 postnatal days for control group and 72.1 ± 1.7 postnatal days in cHet group) were anaesthetized deeply with ketamine–xylazine (ketamine: 100 mg/kg, xylazine: 10 mg/kg), transcardially perfused with 25 mL of ice-cold cutting solution (containing the following in mM: 250 sucrose, 2 KCl, 1.25 NaH2PO4, 26 NaHCO3, 7 MgSO4, 0.5 CaCl2, and 10 glucose, pH 7.4, 330–340 mOsm/L) and decapitated. The brain was then dissected carefully and transferred rapidly into an ice-cold (0–4 °C) cutting solution. Auditory thalamocortical slices (thickness, 350 μm) containing A1 and the medial geniculate nucleus were prepared. For A1 slices, the cutting angle was 15 degrees from the horizontal plane (lateral raised; Cruikshank et al., 2002; Zhao et al., 2009; Meng et al., 2017). Auditory thalamocortical slices were cut in the

previously mentioned ice-cold solution using a vibratome (VT1000S; Leica Microsystems or Microm; Fisher Scientific) and transferred to a heated (37.5 °C) oxygenated recovery solution containing the following (in mM): 124 NaCl, 2.5 KCl, 1.25 NaH2PO4, 26 NaHCO3, 3 MgSO4, 1 CaCl2, and 10 glucose; pH 7.4; 300 mOsm/L, and allowed to recover for 45 min. Subsequently, during experiments, slices were continuously perfused (2 mL/min) with standard artificial cerebrospinal fluid (ACSF) containing the following (in mM): 124 NaCl, 2.5 KCl, 1.25 NaH2PO4, 26 NaHCO3, 2 MgSO4, 2CaCl2, and 10 glucose, pH 7.4 saturated with 95% O2 and 5% CO2 at near physiological temperature (30–33°C). We did not observe any difference between control and cHet mice in terms of slices quality, success rate of recordings and cellular health.

Whole-cell patch clamp recording

PV+ and SST+ neurons located in layer IV of A1 cortex were visually identified as EGFP-expressing somata under an epifluorescence microscope with blue light (filter set: 450–490 nm). All electrophysiological recordings were carried out using a 40x water-immersion objective. Recording pipettes were pulled from borosilicate glass (World Precision Instruments) with a PP-83 two-stage puller (Narishige) to a resistance range of 5–7 MΩ when backfilled with intracellular solution. Whole-cell patch-clamp recordings from PV+ and SST+ interneurons were performed in voltage or current-clamp mode. Pipette capacitance was neutralized, and bridge balance applied. For voltage-clamp recording, we used an intracellular Cs+-based solution containing (in mM): 130 CsMeSO4, 5 CsCl, 2 MgCl2, 10 phosphocreatine, 10 HEPES, 0.5 EGTA, 4 ATP-TRIS, 0.4 GTP-TRIS, 0.3% biocytin, 2 QX-314 (pH 7.2–7.3; 280–290 mOsm/L). These recordings were performed to analyze the excitatory drive received by PV+ and SST+ cells. Series resistance in voltage-clamp were monitored throughout the experiment and cells that had substantial changes in series resistance (>15%) during recording were discarded. The reported voltage values were not compensated for the junction potential. Recordings of sEPSC and mEPSCs were performed in voltage-clamp at –70 mV in the presence of gabazine (1μM; Tocris Bioscience) and CGP55845 (2μM; Abcam Biochemicals).

sEPSCs were first sampled over a 2 min period. A TTX (1μM; Alomone Labs) containing perfusion solution was then added (flow rate of 2 mL/min) and, after a 5 min-interval, mEPSCs were sampled over a 2 min period. Recordings of spontaneous and miniature inhibitory postsynaptic currents (sIPSC, mIPSCs) were performed in voltage-clamp at +10mV in the presence of NBQX (10μM; Abcam Biochemicals) and DL-AP5 (100μM; Abcam Biochemicals) for sISPCs and with addition of TTX (1μM) for mIPSCs. For recordings of thalamocortical electrically evoked AMPA/NMDA EPSC in layer IV PV+ cells, current pulses (2ms duration, 25 to 1000 μA) were delivered to the thalamic radiation every 30 seconds. via a tungsten concentric bipolar microelectrode placed in the white matter midway between the medial geniculate nucleus and the AI (rostral to the hippocampus). Electrical stimulation of thalamic radiation may activate not only monosynaptic thalamic fibers but also polysynaptic (corticothalamic and/or corticocortical) EPSC component. To identify monosynaptic thalamo-cortical connections, we used as criteria the onset latencies of EPSC and the variability jitter obtained from the standard deviation of onset latencies. Onset latencies were defined as the time interval between the beginning of the stimulation artifact and the onset of the EPSC. Monosynaptic connections are characterized by short onset latencies and low jitter variability (Richardson et al., 2009; Blundon et al., 2011; Chun et al., 2013). In our experiments, the initial slopes of EPSCs evoked by white matter stimulation had short onset latencies (mean onset latency, 4.27 ± 0.11 ms, N=16 neurons in controls, and 5.07 ± 0.07 ms, N=14 neurons in cHet mice) and low onset latency variability jitter (0.24 ± 0.03 ms in controls vs 0.31 ± 0.03 ms in cHet mice), suggestive of activation of monosynaptic thalamocortical monosynaptic connections (Richardson et al., 2009; Blundon et al., 2011; Chun et al., 2013). Evoked AMPA (eAMPA) currents were recorded at -70 mV in presence of CGP (2μM) and gabazine (1μM), while evoked NMDA (eNMDA) currents were recorded at +40 mV in presence of NBQX (10μM) and confirmed after with the application of DL-AP5 (100μM). For paired pulse ratio (PPR) experiments, local synaptic stimulation in layer IV was achieved using a bipolar stimulating electrode made from borosilicate theta-glass capillaries (BT-150-10, Sutter Instruments, Novato, CA) filled with ACSF. Two EPSCs

were evoked in layer IV BC with two electric pulses (0.2 ms, 40–140 µA each) at five intervals (30, 50, 100, 200 and 500 ms) every 10 secs in presence of picrotoxin (100 µM; Tocris/Cedarlane).

Current-clamp recordings were obtained in ACSF containing synaptic blockers gabazine (1µM), CGP55845 (2µM) and kynurenic acid (2mM). For these recordings, we used an intracellular K+-based solution containing (in mM): 130 KMeSO4, 2 MgCl2, 10 di-Na-phosphocreatine, 10 HEPES, 4 ATP-Tris, 0.4 GTP-Tris, and 0.3% biocytin (Sigma), pH 7.2–7.3, 280–290 mOsm/L. Passive and active membrane properties were analyzed in current clamp mode: active membrane properties were recorded by subjecting cells to multiple current step injections (step size 40 pA) of varying amplitudes (–200 to 600 pA). In subsequent experiments, the same protocol was repeated in presence of the voltage gated potassium channel (Kv) blocker α-DTX (100nM; Alomone labs). In these experiments, slices were recovered in a holding chamber for at least 1 hr in presence of α-DTX. Once placed in recording chamber slices were kept for recording for max 1 hr. Passive membrane properties, resting membrane potential (Vm), input resistance (Rin), and membrane capacitance (Cm) were obtained immediately after membrane rupture. Membrane potentials were maintained at –80 mV, series resistances (10–18 MΩ) and Rin were monitored on-line with a 40 pA current injection (150ms) given before each 500ms current injection stimulus. Only cells with resting membrane potential more negative than -60mV at the start of recording and spikes with overshoot were considered for further analysis. We performed bridge balance and neutralized the capacitance before starting every recording. The bridge balance was monitored throughout the experiment, and neurons showing changes of >15% in bridge balance during the recording were discarded. Data acquisition (filtered at 2–3 kHz and digitized at 10kHz; Digidata 1440, Molecular Devices, CA, United States) was performed using the Multiclamp 700B amplifier and the Clampex 10.6 software (Molecular Devices).

Electrophysiological data analysis

All analysis was performed by researchers blinds to the genotype. Analysis of electrophysiological recordings was performed using Clampfit 10.7 (Molecular Devices). For the analysis of sEPSCs, mEPSCs, sIPSCs and mIPSCs a minimum of 100 events were sampled per cell over a 2min period using an automated template search algorithm in Clampfit. The 20–80% rise time of the response and the decay time constant determined from the exponential fit (100–37%) were calculated. Charge transfer was calculated by integrating the area under the EPSC and IPSC waveforms. The mean PSC synaptic current was calculated as the charge transfer of the averaged PSC (ΔQ) multiplied by mean PSC frequency. For thalamocortical eAMPA and eNMDA, the mean amplitude of EPSCs including both failure and success was obtained from a total of 5 to 10 sweeps. Onset latency indicated the time from beginning of stimulus artifact and the onset of eAMPA or eNMDA. To measure eNMDA/eAMPA ratios, the eAMPA component was taken at the peak of EPSC at −70 mV, whereas the eNMDA component was measured at the peak of EPSC at +40 mV. For PPR experiments, the PPR was calculated as the ratio between the mean AUC of the second response and the mean AUC of the first response (7 to 10 sweeps).

For the analysis of current-clamp recordings from PV cells, threshold current was measured as the minimal current necessary to evoke an AP. For the analysis of the AP properties, the first AP appearing within a 50ms time window from beginning of current pulse was analyzed. AP latency was measured as the time between current step onset and when membrane voltage reached AP threshold. The AP amplitude was measured from the AP threshold to the peak. The AP half-width was measured at the voltage level of the half of AP amplitude. The AP rise and fall time were measured between the AP threshold and the maximal AP amplitude, and between the maximal AP amplitude and the AP end, respectively. The fast afterhyperpolarization (fAHP) amplitude was determined as the minimum voltage following the AP peak subtracted from the AP threshold. fAHP time was determined as the time between AP threshold and the negative peak of fAHP. The

hyperpolarization-activated cation current (I_h)-associated voltage rectification (I_h sag) was determined as the amplitude of the membrane potential sag from the peak hyperpolarized level to the level at the end of the hyperpolarizing step when the cell was hyperpolarized to –100mV. Membrane time constant (τ) was calculated by the product of R_{in} and C_m. For the firing analysis, we considered only APs with amplitude >30 mV as full APs. Spikelets with amplitude smaller than 30mV were not analyzed in this study. The inter-spike interval (ISI) was determined by the time difference between adjacent AP peaks. Spike amplitude accommodation ratio (AAR) was calculated by dividing the amplitude of the last AP by the amplitude of the first generated in response to 2x threshold current injection. Firing frequency adaptation ratios (FFAR) were calculated by dividing the last ISI with the first one of the responses to 2x threshold current injection. The maximal (initial) firing frequency (F_{max}initial) was computed as the reciprocal of the first ISI in a spike train elicited by the current step (max +600pA) applied before a noticeable appearance of spikelets. The steady-state firing frequency (F_{ss}) was computed as the reciprocal of the average of the last 4 ISIs in the spike train were F_{max}initial was obtained. Finally, the number of APs (# APs)-current relationship for evoked firing was determined by injecting 500-ms somatic current steps of increasing amplitude (40pA increments) to a maximum of 600pA. For current-clamp recordings in presence of α-DTX experiments the delta (Δ) values were calculated for threshold current, AP threshold and AP number at +200pA, by subtracting individual values of α-DTX-treated cells from the average of their respective control group.

Hierarchical clustering and principal component analysis (PCA)

This analysis was based on previous published data finding heterogeneity in PV+ interneurons population (Helm et al., 2013), and performed using the software IBM SPSS V29.0.0. Hierarchical clustering was based on Euclidean distance of PV+ cells from control mice. To identify potential clusters, we used AP half-width and F_{max}initial values. We then performed multidimensional cluster analysis on passive and active membrane properties to identify possible common groupings of PV+

interneurons using the software Prism 9.0 (GraphPad Software). In our database, we focused on 13 parameters (see ***Figure 5b***) that were for the majority unrelated. ***Figure 5b*** is a cross-correlation matrix of these 13 parameters with correlation indices shade-coded. Black means perfectly positively correlated (correlation index of 1.0), white means perfectly negative correlated (correlation index of -1.0) and light gray not correlated (correlation index of 0). In our database, we have parameters that are not strongly correlated (e.g., threshold current and AP amplitude, fAHP amplitude and AP latency), and others that are correlated (correlation coefficient > 0.5 or < -0.5; AP latency and amplitude AR; AP half-width and AP amplitude; Rin and AP half-width; AP amplitude and F_{max} initial). We retained all parameters because they encompass different features of membrane properties (Helm et al., 2013). We therefore performed PCA on the 13 parameters to reduce the dimensionality and to potentiate clusters separation.

Immunohistochemistry, cell reconstruction and anatomical identification

For post-hoc anatomical identification, every recorded neuron was filled with biocytin (0.5%, Sigma) during whole-cell recordings (15 min). To reveal biocytin, the slices were permeabilized with 0.3% triton X-100 and incubated at 4 °C with a streptavidin-conjugated Alexa-488 (1:1000, Invitrogen, Cat# S11223) in TBS. For PV and SST immunofluorescence, sections were permeabilized with 0.25% Triton X-100 in PBS and incubated in blocking solution containing 20% normal goat serum (NGS) for 1 h. Then, sections were incubated with the following primary antibodies diluted in 1% NGS, 0.25% Triton-X 100 in PBS: were incubated with primary antibodies mouse anti-PV (1:1000, Swant, Cat# 235) and rabbit anti-SST (1:1000, Thermofisher Invitrogen, Cat# PA5-82678) at 4°C for 48-72 h. Sections were then washed in PBS (3X- 10 mins each), incubated for 2 hrs at RT with the following secondary antibodies diluted in 1% NGS, 0.25% Triton-X 100 in PBS and mounted on microscope slides: Alexa 555-conjugated goat anti-rabbit (1:1000; Life technologies, A21430) and Alexa 647-conjugated goat anti-mouse (1:250, Cell signaling, 4410S). Whole biocytin-filled cells were acquired with a 1µm step using a 20x objective

(NA 0.75) on a Leica SP8-DLS confocal microscope. For each imaged neuron, we noted the spatial distribution across cortical layers of the axonal arbor and whether its dendrites carried spines. Confocal stacks of PV+ neurons were merged for detailed reconstruction in Neuromantic tracing software version 1.7.5 (Myatt et al., 2012). Dendritic arbors were reconstructed plane-by-plane from the image z-stack and analyzed using the Neuromantic software. All the reconstructions used for dendritic analysis contained intact cells with no evident cut dendrites. Sholl analysis of reconstructed dendritic arbors was performed in FIJI software using the plugin Neuroanatomy. This analysis was performed in radial coordinates, using a 10µm step size from r=0, with the origin centered on the cell soma, and counting the number of compartments crossing a given radius. All analysis was performed by researchers blinds to the genotype.

vGlut1/PSD95 and vGlut 2/PSD immunostaining, imaging and quantification

P60 mice were anesthetized with: Ketamine-100mg/kg+Xylazine-10mg/kg+Acepromazine-10mg/kg and perfused transcardially with 0.9% saline followed by 4% Paraformaldehyde (PFA) in phosphate buffer (0.1M PB, pH 7.2-7.4). Brains were dissected out and post-fixed in 4% PFA overnight at 4°C. They were subsequently transferred to 30% sucrose (prepared in PBS, pH 7.2) at 4°C for 48 hrs. Brains were then embedded in molds filled with OCT Tissue Tek and frozen in a bath of 2-methybutane placed on a bed of dry ice and ethanol. Coronal sections were cut at 40µm with a cryostat (Leica CM3050 S) and collected as floating sections in PBS. Brain sections were first permeabilized in 0.2 % Triton-X in PBS for 1 hr at RT and then blocked in 10% normal donkey serum (NDS) with 0.2% Triton-X 100 and 5% bovine serum albumin (BSA) in PBS for 2 hrs at RT followed by incubation at 4°C for 48 hrs with the following primary antibodies diluted in 5% NDS, 0.2% Triton-X 100 and 2 % BSA in PBS: goat anti-PV (1:1000, Swant, Cat# PVG-213), rabbit anti-VGlut1 (1:100 Thermo Fisher/ Invitrogen, Cat# 48-2400), rabbit anti-VGlut2 1:1000, Synaptic systems, Cat# 135402) mouse anti-PSD95 (1:500, Invitrogen, Cat# MA1-05). Sections were then washed in PBS + 0.1% Triton-X 100 (3X10 mins each) and incubated for 2 hrs at RT with the

following secondary antibodies diluted in 5% NDS, 0.2% Triton-X 100 and 2 % BSA in PBS : Alexa 488-conjugated donkey anti-rabbit (1:500, Life technologies/ Invitrogen, Cat# A11055), Alexa 555-conjugated donkey anti-mouse (1:500, Life technologies/ Invitrogen, Cat# A31570), Alexa 633-conjugated donkey anti-goat (1:500, Invitrogen, Cat# A21082). Sections were rinsed in 0.1% Triton-X 100 in PBS (3X10' each +1X5') and mounted with Vectorshield mounting medium (Vector).

Immunostained sections were imaged using a Leica SP8-STED confocal microscope, with an oil immersion 63x (NA 1.4) at 1024 X 1024, zoom=1, z-step =0.3 µm, stack size of ~15 µm. Images were acquired from the A1 from at least 3 coronal sections per animal. All the confocal parameters were maintained constant throughout the acquisition of an experiment. All images shown in ***Suppl. Figure 3a,c*** are from a single confocal plane. To quantify the number of vGlut1/PSD95 or vGlut2/PSD95 putative synapses, images were exported as TIFF files and analyzed using Fiji (Image J) software. We first manually outlined the profile of each PV cell soma (identified by PV immunolabeling). At least 4 innervated somata were selected in each confocal stack. We then used a series of custom-made macros in Fiji as previously described (Chehrazi et al, 2023). After subtracting background (rolling value = 10) and Gaussian blur (σ value = 2) filters, the stacks were binarized and vGlut1/PSD95 or vGlut2/PSD95 puncta were independently identified around the perimeter of a targeted soma in the focal plane with the highest soma circumference. Puncta were quantified after filtering particles for size (included between 0-2µm2) and circularity (included between 0-1). Quantification of the density of perisomatic puncta colocalizing both VGlut1-PSD95 and VGlut2-PSD95 were normalised to controls. All analysis was performed by researchers blinds to the genotype. No mouse was excluded from this analysis.

Statistics

Data were expressed as mean±SEM. For statistical analysis, we based our conclusion on the statistical results generated by LMM, modelling animal as a random effect and genotype as fixed

effect. We used this statistical analysis because we considered the number of mice as independent replicates and the number of cells in each mouse as repeated measures (Berryer et al. 2016; Heggland et al., 2019; Yu et al., 2022). For cumulative distributions, the same number of events was chosen randomly from each cell and analysed by LMM, modelling animal as a random effect and genotype as fixed effect. Two-way ANOVA with Sidak's multiple comparison post hoc test was used for the detection of differences in AP firing and number of dendritic intersections between genotypes. Statistical analysis was performed using Sigma Plot 11.0, Prism 9.0 (GraphPad Software) and IBM SPSS V29.0.0 for LMM analysis.

ACKNOWLEDGEMENTS. We are very grateful to Dr Lisa Topolnik for her invaluable suggestions and help. We would like to thank James Bellord Waldron for his technical assistance, the Comité Institutionnel de Bonne Pratiques Animales en Recherche (CIBPAR), all the personnel of the animal facility of the Research Center of CHU Sainte-Justine (Université de Montreal), Compute Canada and the Plateforme Imagerie Microscopique (PIM) of the Research Center of CHU Sainte-Justine for their instrumental technical support and all lab members for insightful data discussion. This work was supported by the Canadian Institutes of Health Research (G.DC, S.K.), Natural Sciences and Engineering Research Council of Canada (S.K.), Rare Diseases: Model and Mechanisms Network (G.DC), Jonathan-Bouchard Chair in intellectual disability (J.L.M.) and Fonds UdeM pour le partenariat CHU Sainte-Justine -Institut Imagine en épilepsie de l'enfant (G.DC, J.L.M.). R.F. is supported by Fonds de Recherche du Québec en Santé (FRQS), and Savoy Foundation fellowship.

References

Aarts E, Verhage M, Veenvliet J, Dolan CV, van der Sluis S (2014) **A solution to dependency: using multilevel analysis to accommodate nested data.** *Nature Neuroscience* **17**:491–496 https://doi.org/10.1038/nn.3648

Aceti M, Creson TK, Vaissiere T, Rojas C, Huang WC., Wang YX, Petralia RS, Page DT, Miller CA, Rumbaugh G (2015) **Syngap1 Haploinsufficiency damages a postnatal critical period of pyramidal cell structural maturation linked to cortical circuit assembly** *Biological Psychiatry* **77**:805–815 https://doi.org/10.1016/j.biopsych.2014.08.001

Araki Y, Zeng M, Zhang M, Huganir RL (2015) **Rapid dispersion of SynGAP from synaptic spines triggers AMPA receptor insertion and spine enlargement during LTP** *Neuron* **85**:173–189 https://10.1016/j.neuron.2014.12.023

Arora V, Michaelson S, Aceti M, Kilinic M, Miller C, Rumbaugh, G (2022) **Syngap1 regulates cortical circuit assembly by controlling membrane excitability** *BioRxiv* https://doi.org/10.1101/2022.12.06.519295

Bengtsson Gonzales C, Hunt S, Munoz-Manchado AB, McBain CJ, Hjerling-Leffler J (2020) **Intrinsic electrophysiological properties predict variability in morphology and connectivity among striatal Parvalbumin-expressing Pthlh-cells** *Scientific Reports* **10**:15680 https://doi.org/10.1038/s41598-020-72588-1

Berryer MH, Chattopadhyaya B, Xing P, Riebe I, Bosoi C, Sanon N, Antoine-Bertrand J, Lévesque M, Avoli M, Hamdan FF, Carmant L, Lamarche-Vane N, Lacaille JC, Michaud JL, Di Cristo G (2016) **Decrease of SYNGAP1 in GABAergic cells impairs inhibitory synapse connectivity, synaptic inhibition and cognitive function** *Nature Communications* **7**:13340 https://doi.org/10.1038/ncomms13340

Berryer MH, Hamdan FF, Klitten LL, Møller RS, Carmant L, Schwartzentruber J, Patry L, Dobrzeniecka S, Rochefort D, Neugnot-Cerioli M, Lacaille JC, Niu Z, Eng CM, Yang Y, Palardy S, Belhumeur C, Rouleau GA, Tommerup N, Immken L, Beauchamp MH, Patel GS, Majewski J, Tarnopolsky MA, Scheffzek K, Hjalgrim H, Michaud JL, Di Cristo G (2013) **Mutations in SYNGAP1 cause intellectual disability, autism, and a specific form of epilepsy by inducing haploinsufficiency** *Human Mutation* **34**:385–394 https://doi:10.1002/humu.22248

Bertero A, Feyen PLC, Zurita H, Apicella A (2019) **A non-canonical cortico-amygdala inhibitory loop** *Journal of Neuroscience* **39**:8424–8438 https://doi.org/10.1523/JNEUROSCI.1515-19.2019

Bertero A, Zurita H, Normandin M, Apicella AJ (2020) **Auditory long-range parvalbumin cortico-striatal neurons** *Frontiers in neural circuits* **14**:45 https//doi: 10.3389/fncir.2020.00045

Birtele M, Del Dosso A, Xu T, Nguyen T, Wilkinson B, Hosseini N, Nguyen S, Urenda JP, Knight G, Rojas C, Flores I, Atamian A, Moore R, Sharma R, Pirrotte P, Ashton RS, Huang EJ, Rumbaugh G, Coba MP, Quadrato G (2023) **Non-synaptic function of the autism spectrum disorder-associated gene SYNGAP1 in cortical neurogenesis** *Nature Neuroscience* **26**:2090-2103 doi: 10.1038/s41593-023-01477-3.

Blundon JA, Bayazitov IT, Zakharenko SS (2011). **Presynaptic gating of postsynaptically expressed plasticity at mature thalamocortical synapses** *The Journal of Neuroscience* **31**:16012-25 https//doi: 10.1523/JNEUROSCI.3281-11.2011

Bourdeau ML, Morin F, Laurent CE, Azzi M, Lacaille JC (2007) **Kv4. 3-mediated A-type K+ currents underlie rhythmic activity in hippocampal interneurons** *The Journal of Neuroscience* **27**:1942– 1953 https://doi.org/10.1523/JNEUROSCI.3208-06.2007

Cardin JA, Carlén M, Meletis K, Knoblich U, Zhang F, Deisseroth K, Tsai LH, Moore CI (2009) **Driving fast-spiking cells induces gamma rhythm and controls sensory responses** *Nature* **459**: 663–667 https:// doi.org/10.1038/nature08002

Carlén M, Meletis K, Siegle JH, Cardin JA, Futai K, Vierling-Claassen D, Rühlmann C, Jones SR, Deisseroth K, Sheng M, Moore CI, Tsai LH (2012) **A critical role for NMDA receptors in parvalbumin interneurons for gamma rhythm induction and behavior** *Molecular Psychiatry* **17**:537–548 https://doi.org/10.1038/mp.2011.31

Carreño-Muñoz MI, Chattopadhyaya B, Agbogba K, Côté V, Wang S, Lévesque M, Avoli M, Michaud JL, Lippé S, Di Cristo G (2022) **Sensory processing dysregulations as reliable translational biomarkers in syngap1 haploinsufficiency** *Brain* **145**:754–69 https://doi.org/10.1093/brain/awab329

Chehrazi P, Lee KKY, Lavertu-Jolin M, Abbasnejad Z, Carreño-Muñoz MI, Chattopadhyaya B, Di Cristo G (2023) **The p75 neurotrophin receptor in preadolescent prefrontal parvalbumin interneurons promotes cognitive flexibility in adult mice** *Biological Psychiatry* **94**:310-321 https:doi.org/10.1016/j.biopsych.2023.04.019

Chiu CQ, Lur G, Morse TM, Carnevale NT, Ellis-Davies GCR, Higley MJ (2013) **Compartmentalization of GABAergic inhibition by dendritic spines** *Science* **340**:759–762 https://doi.org/10.1126/science.1234274

Chun S, Bayazitov IT, Blundon JA, Zakharenko SS (2013) **Thalamocortical long-term potentiation becomes gated after the early critical period in the auditory cortex** *The Journal of Neuroscience* **33**:7345-57 https://doi: 10.1523/JNEUROSCI.4500-12.2013

Clement JP, Aceti M, Creson TK, Ozkan ED, Shi Y, Reish NJ, Almonte AG, Miller BH, Wiltgen BJ, Miller CA, Xu X, Rumbaugh G (2012) **Pathogenic SYNGAP1 mutations impair cognitive development by disrupting maturation of dendritic spine synapses** *Cell* **151**:709-723 https://doi.org/10.1016/j.cell.2012.08.045

Clement JP, Ozkan ED, Aceti M, Miller CA, Rumbaugh G (2013) **SYNGAP1 links the maturation rate of excitatory synapses to the duration of critical-period synaptic plasticity** *The Journal of Neuroscience* **33**:10447-10452 https://doi.org/10.1523/JNEUROSCI.0765-13.2013

Cruikshank SJ, Rose HJ, Metherate R (2002) **Auditory thalamocortical synaptic transmission in vitro** *Journal of Neurophysiology* **87**:361-384 https://doi:10.1152/jn.00549.2001

Dehorter N, Ciceri G, Bartolini G, Lim L, del Pino I, Marín O (2015) **Tuning of fast-spiking interneuron properties by an activity-dependent transcriptional switch** *Science* **349**:1216–1220 https://doi.org/10.1126/science.aab3415

Ekins TG, Mahadevan V, Zhang Y, D'Amour JA, Akgül G, Petros TJ, McBain CJ (2020) **Emergence of non-canonical parvalbumin-containing interneurons in hippocampus of a murine model of type I lissencephaly** *eLife* **9**:e62373 https://doi.org/10.7554/eLife.62373

Elabbady L, Seshamani S, Mu S, Mahalingam G, Schneider-Mizell CM, Bodor AL, Bae JA, Brittain D, Buchanan J, Bumbarger DJ, Castro MA, Dorkenwald S, Halageri S, Jia Z, Jordan C, Kapner D, Kemnitz N, Kinn S, Lee K, Li K, Lu R, Macrina T, Mitchell E, Mondal SS, Nehoran B, Popovych S, Silversmith W, Takeno M, Torres R, Turner NL, Wong W, Wu J, Yin W, Yu SC, Seung HS, Reid RC, da Costa NM, Collman F (2025) **Perisomatic ultrastructure efficiently classifies cells in mouse cortex** *Nature* **640**:478–486 https://doi.org/10.1038/s41586-024-07765-7

Favuzzi E, Marques-Smith A, Deogracias R, Winterflood CM, Sánchez-Aguilera A, Mantoan L, Maeso P, Fernandes C, Ewers H, Rico B (2017) **Activity-dependent gating of parvalbumin interneuron function by the perineuronal net protein brevican** *Neuron* **95**:639-655.e10 https://doi.org/10.1016/j.neuron.2017.06.028

Gamache TR, Araki Y, Huganir RL (2020**) Twenty years of SynGAP research: from synapses to cognition** *The Journal of Neuroscience* **40**:1596-1605 https://doi.org/10.1523/JNEUROSCI.0420-19.2020

Goldberg EM, Clark BD, Zagha E, Nahmani M, Erisir A, Rudy B (2008) **K+ Channels at the axon initial segment dampen near-threshold excitability of neocortical fast-spiking GABAergic interneurons** *Neuron* **58**:387–400 https://doi.org/10.1016/j.neuron.2008.03.003

Golomb D, Donner K, Shacham L, Shlosberg D, Amitai Y, Hansel D. (2007). **Mechanisms of firing patterns in fast-spiking cortical interneurons.** *PLoS Computational Biology* **38** e156 http://doi.org/10.1371/journal.pcbi.0030156

Gothner T, Gonçalves PJ, Sahani M, Linden JF, Hildebrandt KJ (2021) **Sustained activation of PV+ interneurons in core auditory cortex enables robust divisive gain control for complex and naturalistic stimuli** *Cerebral Cortex* **31**:2364-2381 https://doi:10.1093/cercor/bhaa347

Gou G, Roca-Fernandez A, Kilinc M, Serrano E, Reig-Viader R, Araki Y, Huganir RL, Schmidt C, Rumbaugh G, Bayés À (2020) **SynGAP splice variants display heterogeneous spatio-temporal expression and subcellular distribution in the developing mammalian brain** *Journal of Neurochemistry* **154**:618-634 https://doi:10.1111/jnc.14988

Hamdan FF, Gauthier J, Spiegelman D, Noreau A, Yang Y, Pellerin S, Dobrzeniecka S, Côté M, Perreau-Linck E, Carmant L, D'Anjou G, Fombonne É, Addington AM, Rapoport JL, Delisi LE, Krebs MO, Mouaffak F, Joober R, Mottron L, Drapeau P, Marineau C, Lafreniere RG, Lacaille JC, Rouleau GA, Michaud JL (2009) **Mutations in SYNGAP1 in autosomal nonsyndromic mental retardation** *New England Journal of Medicine* **360**:599–605 https://doi.org/10.1056/NEJMoa0805392

Heggland I, Kvello P, Witter MP (2019) **Electrophysiological Characterization of Networks and Single Cells in the Hippocampal Region of a Transgenic Rat Model of Alzheimer's Disease** *ENeuro* **6**: ENEURO.0448-17.2019 https://doi.org/10.1523/ENEURO.0448-17.2019

Helm J, Akgul G, Wollmuth LP (2013) **Subgroups of parvalbumin-expressing interneurons in layers 2/3 of the visual cortex** *Journal of Neurophysiology* **109**:1600–1613 https://doi.org/10.1152/jn.00782.2012

Hostetler RE, Hu H, Agmon A (2023) **Genetically defined subtypes of somatostatin-containing cortical interneurons** *eNeuro* **10**:ENEURO.0204-23.2023 https://doi:10.1523/ENEURO.0204-23.2023

Hwang YS, Maclachlan C, Blanc J, Dubois A, Petersen CCH, Knott G, Lee SH (2021) **3D Ultrastructure of synaptic inputs to distinct GABAergic neurons in the mouse primary visual cortex** *Cerebral Cortex* **31**:2610–2624 https://doi.org/10.1093/cercor/bhaa378

Jadhav V, Carreno-Munoz MI, Chehrazi P, Michaud JL, Chattopadhyaya B, Di Cristo G (2024) **Developmental Syngap1 haploinsufficiency in medial ganglionic eminence-derived interneurons impairs auditory cortex activity, social behavior and extinction of fear memory** *The Journal of Neuroscience* **44**:e0946242024 https://doi:10.1523/JNEUROSCI.0946-24.2024

Ji X, Zingg B, Mesik L, Xiao Z, Zhang LI, Tao HW (2016) **Thalamocortical innervation pattern in mouse auditory and visual cortex: laminar and cell-type specificity** *Cerebral Cortex* **26**: 2612–2625 https://doi.org/10.1093/cercor/bhv099

Kavalali E (2015) **The mechanisms and functions of spontaneous neurotransmitter release** *Nature Reviews Neuroscience* **16**:5–16. https://doi.org/10.1038/nrn3875

Kawaguchi Y, Kubota Y (1997) **GABAergic cell subtypes and their synaptic connections in rat frontal cortex** *Cerebral Cortex* **7**:476–486 https://doi.org/10.1093/cercor/7.6.476

Kawaguchi Y, Karube F, Kubota Y (2006) **Dendritic branch typing and spine expression patterns in cortical nonpyramidal cells** *Cerebral Cortex* **16**:696–711 https://doi.org/10.1093/cercor/bhj015

Keller CH, Kaylegian K, Wehr M (2018) **Gap encoding by parvalbumin-expressing interneurons in auditory cortex** *Journal of Neurophysiology* **120**:105–114 https://doi.org/10.1152/jn.00911.2017

Khlaifia A, Jadhav V, Danik M, Badra T, Berryer MH, Dionne-Laporte A, Chattopadhyaya B, Di Cristo G, Lacaille JC, Michaud JL (2023) **Disruption induced by recombination between inverted loxP sites is associated with hippocampal interneuron dysfunction** *Eneuro*, **10**: ENEURO.0475-22.2023. https://doi.org/10.1523/ENEURO.0475-22.2023

Kim JH, Liao D, Lau LF, Huganir RL (1998) **SynGAP: a synaptic RasGAP that associates with the PSD-95/SAP90 protein family** *Neuron* **20**:683–691 https://doi:10.1016/S0896-6273(00)81008-9 pmid:9581761

Kourdougli N, Suresh A, Liu B, Juarez P, Lin A, Chung DT, Graven Sams A, Gandal MJ, Martínez-Cerdeño V, Buonomano DV, Hall BJ, Mombereau C, Portera-Cailliau C (2023) **Improvement of sensory deficits in fragile X mice by increasing cortical interneuron activity after the critical period** *Neuron* **111**:2863-2880 https://doi.org/10.1016/j.neuron.2023.06.009

Levy RB, Reyes AD (2012) **Spatial profile of excitatory and inhibitory synaptic connectivity in mouse primary auditory cortex** *The Journal of Neuroscience* **32**:5609-5619 https://doi.org/10.1523/JNEUROSCI.5158-11.2012

Li L, Ji X, Liang F, Li Y, Xiao Z, Tao HW, Zhang LI (2014) **A feedforward inhibitory circuit mediates lateral refinement of sensory representation in upper layer 2/3 of mouse primary auditory cortex** *The Journal of Neuroscience* **34**:13670-13683

https://doi.org/10.1523/JNEUROSCI.1516-14.2014

McMahon AC, Barnett MW, O'Leary TS, Stoney PN, Collins MO, Papadia S, Choudhary JS, Komiyama NH, Grant SGN, Hardingham GE, Wyllie DJA, Kind PC (2012) **SynGAP isoforms**

exert opposing effects on synaptic strength *Nature Communications*, **3**:900 https://doi:10.1038/ncomms1900

Meng X, Kao JPY, Lee HK, Kanold PO (2017) **Intracortical circuits in thalamorecipient layers of auditory cortex refine after visual deprivation** *Eneuro* **4**:ENEURO.0092-17.2017 https://doi.org/10.1523/ENEURO.0092-17.2017

Michaelson SD, Ozkan ED, Aceti M, Maity S, Llamosas N, Weldon M, Mizrachi E, Vaissiere T, Gaffield MA, Christie JM, Holder JL, Miller CA, Rumbaugh G (2018) **SYNGAP1 heterozygosity disrupts sensory processing by reducing touch-related activity within somatosensory cortex circuits** *Nature Neuroscience* **21**:1–13 https://doi.org/10.1038/s41593-018-0268-0

Moon IS, Sakagami H, Nakayama J, Suzuki T (2008) **Differential distribution of synGAP alpha1 and synGAP beta isoforms in rat neurons** *Brain Research* **1241**:62–75 https://doi.org/10.1016/j.brainres.2008.09.033

Moore, A K, Wehr M (2013) **Parvalbumin-expressing inhibitory interneurons in auditory cortex are well-tuned for frequency** *The Journal of Neuroscience* **33**:13713-13723 https://doi:10.1523/JNEUROSCI.0663-13.2013

Myatt D, Hadlington T, Ascoli G, Nasuto S (2012) **Neuromantic – from semi-manual to semi-automatic reconstruction of neuron morphology** *Frontiers in Neuroinformatics* **6**:4 https://doi:10.3389/fninf.2012.00004

Nassar M, Simonnet J, Lofredi R, Cohen I, Savary E, Yanagawa Y, Miles R, Fricker D (2015) **Diversity and overlap of Parvalbumin and Somatostatin expressing interneurons in mouse presubiculum** *Frontiers in Neural Circuits* **9**:20 https://doi:10.3389/fncir.2015.00020

Okaty BW, Miller MN, Sugino K, Hempel CM, Nelson SB (2009) **Transcriptional and electrophysiological maturation of neocortical fast-spiking GABAergic interneurons** *The Journal of Neuroscience* **29**:7040-7052 https://doi:10.1523/JNEUROSCI.0105-09.2009

Ozkan ED, Creson TK, Kramár EA, Rojas C, Seese RR, Babyan AH, Shi Y, Lucero R, Xu X, Noebels JL, Miller CA, Lynch G, Rumbaugh G (2014) **Reduced cognition in Syngap1 mutants is caused by isolated damage within developing forebrain excitatory neurons** *Neuron* **82**:1317–1333 https://doi.org/10.1016/j.neuron.2014.05.015

Phillips EAK, Hasenstaub AR (2016) **Asymmetric effects of activating and inactivating cortical interneurons** *eLife* **5**:e18383 https://doi.org/10.7554/eLife.18383.

Porter K, Komiyama NH, Vitalis T, Kind PC, Grant SG (2005) **Differential expression of two NMDA receptor interacting proteins, PSD-95 and SynGAP during mouse development** *European Journal of Neuroscience* **21**:351–362 https://doi.org/10.1111/j.1460-9568.2005.03874.x

Povysheva NV, Gonzalez-Burgos G, Zaitsev AV, Kröner S, Barrionuevo G, Lewis DA, Krimer LS (2006) **Properties of excitatory synaptic responses in fast-spiking interneurons and pyramidal cells from monkey and rat prefrontal cortex** *Cerebral Cortex* **16**:541–552 https://doi.org/10.1093/cercor/bhj002

Ramirez DM, Kavalali ET (2011) **Differential regulation of spontaneous and evoked neurotransmitter release at central synapses** *Current Opinion in Neurobiology* **21**:275-282 https://doi:10.1016/j.conb.2011.01.007

Richardson RJ, Blundon JA, Bayazitov IT, Zakharenko SS (2009) **Connectivity patterns revealed by mapping of active inputs on dendrites of thalamorecipient neurons in the auditory cortex** *The Journal of Neuroscience* **29**:6406-17 https://doi: 10.1523/JNEUROSCI.0258-09.2009.

Riedemann T, Straub T, Sutor B (2018) **Two types of somatostatin-expressing GABAergic interneurons in the superficial layers of the mouse cingulate cortex** *PLoS One* **13**:e0200567 https://doi: 10.1371/journal.pone.0200567.

Rock C, Zurita H, Lebby S, Wilson CJ, Apicella AJ (2018) **Cortical circuits of callosal GABAergic neurons** *Cerebral Cortex* **28**:1154–1167 https://doi.org/10.1093/CERCOR/BHX025

Rudy B, Fishell G, Lee S, Hjerling-Leffler J (2011). **Three groups of interneurons account for nearly 100% of neocortical GABAergic neurons** *Developmental Neurobiology* **71**:45–61 https://doi: 10.1002/dneu.20853

Rumbaugh G, Adams JP, Kim JH, Huganir RL (2006) **SynGAP regulates synaptic strength and mitogen-activated protein kinases in cultured neurons** *Proceedings of the National Academy of Sciences* **103**:4344–4351 https://doi.org/10.1073/pnas.0600084103

Sara Y, Virmani T, Deák F, Liu X, Kavalali ET (2005) **An isolated pool of vesicles recycles at rest and drives spontaneous neurotransmission** *Neuron* **45**:563-573 https://doi:10.1016/j.neuron.2004.12.056

Sara Y, Bal M, Adachi M, Monteggia LM, Kavalali ET (2011) **Use-dependent AMPA receptor block reveals segregation of spontaneous and evoked glutamatergic neurotransmission** *Journal of Neuroscience* **14**:5378-5382 https://doi.org/10.1523/JNEUROSCI.5234-10.2011

Scala F, Kobak D, Shan S, Bernaerts Y, Laturnus S, Cadwell CR, Hartmanis L, Froudarakis E, Castro JR, Tan ZH, Papadopoulos S, Patel SS, Sandberg R, Berens P, Jiang X,Tolias AS (2019) **Layer 4 of mouse neocortex differs in cell types and circuit organization between sensory areas** *Nature Communications* **10**:4174 https://doi.org/10.1038/s41467-019-12058-z

Serôdio P, Rudy B (1998) **Differential expression of Kv4 K+ channel subunits mediating subthreshold transient K+ (A-type) currents in rat brain** *Journal of Neurophysiology* **79**:1081–1091 https://doi.org/10.1152/jn.1998.79.2.1081

Seybold BA, Phillips EAK, Schreiner CE, Hasenstaub AR (2015) **Inhibitory actions unified by network integration** *Neuron* **87**:1181–1192 https://doi.org/10.1016/j.neuron.2015.09.013

Spencer K (2012) **Baseline gamma power during auditory steady-state stimulation in schizophrenia** *Frontiers in Human Neuroscience* **5**:190 https://doi.org/10.3389/fnhum.2011.00190

Studer F, Barkat TR (2022) **Inhibition in the auditory cortex** *Neuroscience and Biobehavioral Reviews* **132**:61–75 https://doi.org/10.1016/J.NEUBIOREV.2021.11.021

Stevens SR, Longley CM, Ogawa Y, Teliska LH, Arumanayagam AS, Nair S, Oses-Prieto JA, Burlingame AL, Cykowski MD, Xue M, Rasband MN (2021) **Ankyrin-R regulates fast-spiking interneuron excitability through perineuronal nets and Kv3.1b K+ channels** *Elife* **10**:e66491 http://doi.org/10.7554/eLife.66491

Su P, Lai TKY, Lee FHF, Abela AR, Fletcher PJ, Liu F (2019) **Disruption of SynGAP–dopamine D1 receptor complexes alters actin and microtubule dynamics and impairs GABAergic interneuron migration** *Science Signaling* **12**:eaau9122 https://doi.org/10.1126/scisignal.aau9122

Sullivan BJ, Ammanuel S, Kipnis PA, Araki Y, Huganir RL, Kadam SD (2020) **Low-dose perampanel rescues cortical gamma dysregulation associated with parvalbumin interneuron GluA2 upregulation in epileptic Syngap1+/− mice** *Biological Psychiatry* **87**:829-842 https://doi.org/10.1016/j.biopsych.2019.12.025

Tremblay R, Lee S, Rudy B (2016) **GABAergic interneurons in the neocortex: from cellular properties to circuits** *Neuron* **91**:260–292 https://doi.org/10.1016/j.neuron.2016.06.033

Velmeshev D, Schirmer L, Jung D, Haeussler M, Perez Y, Mayer S, BhaduriA, Goyal N, Rowitch DH, Kriegstein AR (2019) **Single-cell genomics identifies cell type-specific molecular changes in autism** *Science* **364**:685–689 https:// doi: 10.1126/science.aav8130

Vermaercke B, Iwata R, Wierda K, Boubakar L, Rodriguez P, Ditkowska M, Bonin V, Vanderhaeghen P (2024) **SYNGAP1 deficiency disrupts synaptic neoteny in xenotransplanted human cortical neurons in vivo** *Neuron* https://doi:10.1016/j.neuron.2024.07.007

Wang H, Kunkel DD, Schwartzkroin PA, Tempel BL (1994) **Localization of Kv1.1 and Kv1.2, two K channel proteins, to synaptic terminals, somata, and dendrites in the mouse brain** *The Journal of Neuroscience* **14**:4588-4599 https://doi.org/10.1523/JNEUROSCI.14-08-04588.1994

Wehr M, Zador AM (2003) **Balanced inhibition underlies tuning and sharpens spike timing in auditory cortex** *Nature* **426**:442–446 https://doi.org/10.1038/nature02116

Wilkinson B, Li J, Coba MP (2017) **Synaptic GAP and GEF Complexes Cluster Proteins Essential for GTP Signaling** Scientific Reports **7**:5272 https://doi: 10.1038/s41598-017-05588-3

Xu Q, Tam M, Anderson SA (2008) **Fate mapping Nkx2.1-lineage cells in the mouse telencephalon** *Journal of Comparative Neurology* **506**:16-29 https://10.1002/cne.21529

Yavorska I, Wehr M (2016) **Somatostatin-expressing inhibitory interneurons in cortical circuits** *Frontiers in Neural Circuits*, **10**:76 https://doi.org/10.3389/fncir.2016.00076

Yee JX, Rastani A, Soden ME (2022) **The potassium channel auxiliary subunit Kvβ2 (Kcnab2) regulates Kv1 channels and dopamine neuron firing** *Journal of Neurophysiology* **128**:62–72 https://doi.org/10.1152/jn.00194.2022

Yu Z, Guindani M, Grieco SF, Chen L, Holmes TC, Xu X (2022) **Beyond t test and ANOVA: applications of mixed-effects models for more rigorous statistical analysis in neuroscience research** *Neuron* **110**:21-35 https://doi: 10.1016/j.neuron.2021.10.030

Zhang W, Vazquez L, Apperson M, Kennedy MB (1999) **Citron binds to PSD-95 at glutamatergic synapses on inhibitory neurons in the hippocampus** *The Journal of Neuroscience*, **19**:96-108. https://doi.org/10.1523/JNEUROSCI.19-01-00096.1999

Zhao C, Kao JPY, Kanold PO (2009) **Functional excitatory microcircuits in neonatal cortex connect thalamus and layer 4** *The Journal of Neuroscience* **29**:15479-15488 https://doi.org/10.1523/JNEUROSCI.4471-09.2009

Zhao M, Kwon SE (2023) **Interneuron-targeted disruption of SYNGAP1 alters sensory representations in the neocortex and impairs sensory learning** *The Journal of Neuroscience* **43**: 6212-6226 https://doi:10.1523/JNEUROSCI.1997-22.2023

Zurita H, Feyen PLC, Apicella AJ (2018) **Layer 5 callosal parvalbumin-expressing neurons: a distinct functional group of GABAergic neurons** *Frontiers in Cellular Neuroscience* **12**:53 https://doi.org/10.3389/fncel.2018.00053

Figures

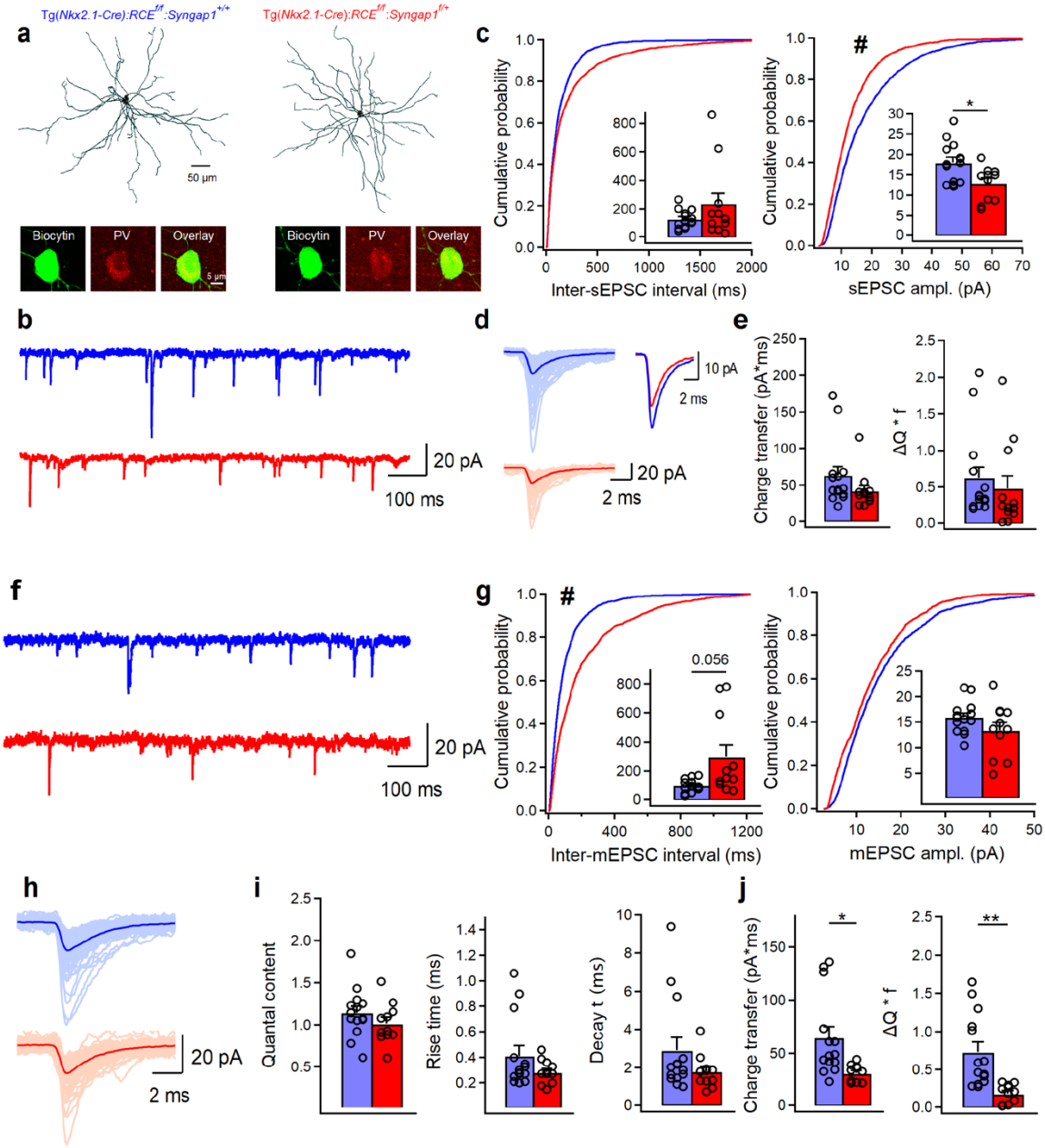

Figure 1. *Syngap1* haploinsufficiency in Nkx2.1+ interneurons is associated with reduced sEPSC amplitude and mEPSC frequency in LIV BCs. (a) Anatomical reconstructions of PV+ cells filled with biocytin in control (left) and cHet mice (right) during whole-cell patch-clamp recordings and post hoc immunohistochemical validation of BC interneurons confirming the positivity for PV. (**b**) Representative traces of sEPSCs recorded in BCs cells from control Tg(*Nkx2.1-Cre*)*:RCE*$^{f/f}$*:Syngap1*$^{+/+}$ (blue, n=14 cells, 7 mice) and cHet Tg(*Nkx2.1-*

Cre):*RCE*$^{f/f}$:*Syngap*$^{f/+}$ (red, n=11 cells, 6 mice) mice. (**c**) Cumulative probability plots show a significant decrease in the amplitude of sEPSC in cHet mice compared to control mice (hash sign denote the significance for LMM related to the cumulative distributions ,# p=0.029) and no change in the inter-sEPSC interval (LMM, p=0.345). Insets illustrate significant differences in the sEPSC amplitude for inter-cell mean comparison (LMM, *p=0.014) and no difference for inter-sEPSC interval (LMM, p=0.230). (**d**) Representative examples of individual sEPSC events (100 pale sweeps) and average traces (bold trace) detected in BCs of control and cHet mice and superimposed scaled traces (right top), (**e**) Summary bar graphs showing no differences for inter-cell mean charge transfer (LMM, p=0.090, left) and for the charge transfer when frequency of events is considered (LMM, p=0.140). (**f**) Representative traces of mEPSCs recorded from the same neurons shown in b-e. (**g**) Cumulative probability plots show no change in the amplitude of mEPSC (LMM, p=0.151) and a significant increase in the inter-mEPSC interval in cHet mice compared to control mice (LMM, #p=0.045). Insets illustrate summary data showing no significant differences in the amplitude (LMM, p=0.155) and a trend towards longer inter-mEPSCs intervals for inter-cell mean comparison in cHet compared to control mice (LMM, p=0.056). (**h**) Representative examples of individual mEPSC events (100 pale sweeps) and average traces (bold trace) detected in BCs of control and cHet mice. (**i**) Summary bar graphs for a group of cells show no significant differences in the quantal content (LMM, p=0.189) and mEPSCs kinetics (LMM, p=0.269 for rise time, and p=0.193 for decay time). (**j**) Summary bar graphs showing a significant decrease in cHet mice for inter-cell mean charge transfer (LMM, *p=0.012, left) and for the charge transfer when frequency of events is considered (LMM, **p=0.002). * and # indicates p value <0.05 for bar graphs and cumulative distribution, respectively.

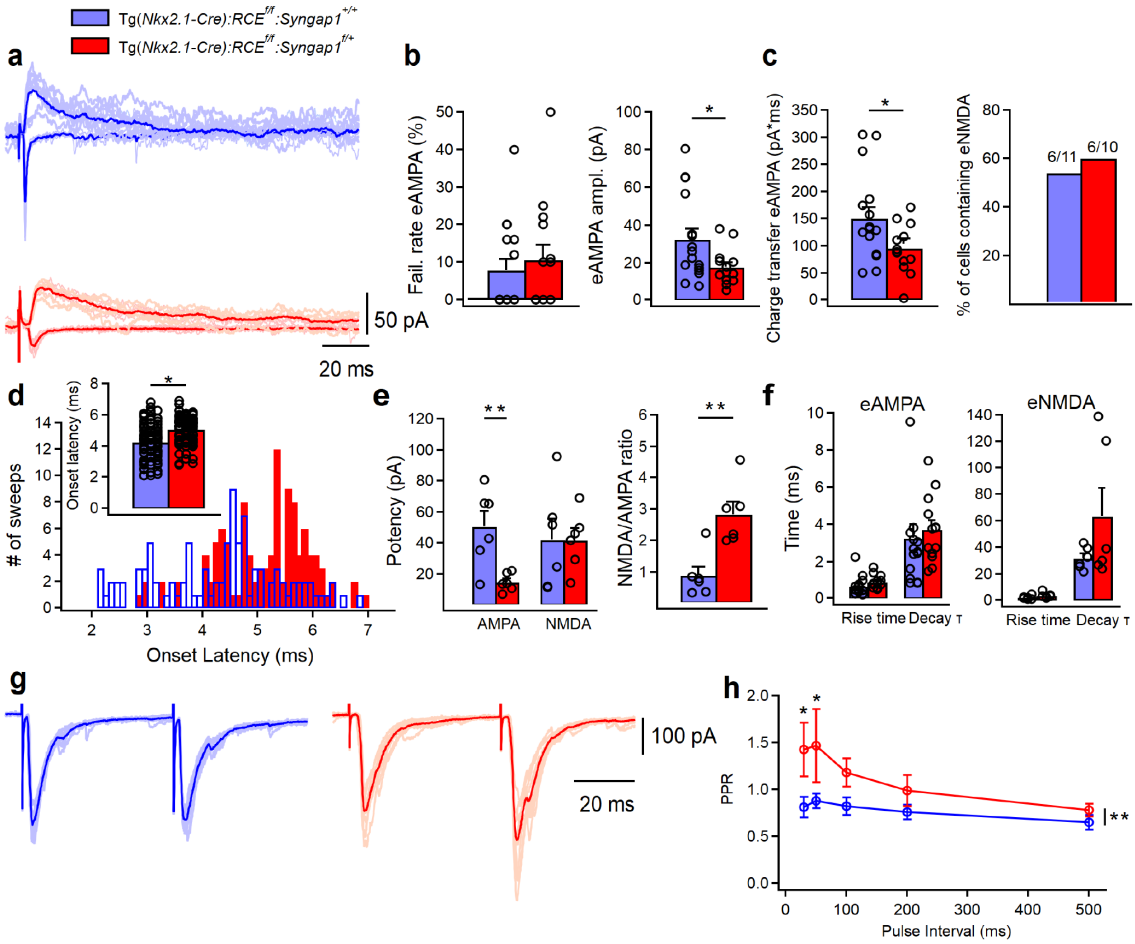

Figure 2. Thalamocortical eAMPA transmission is decreased in LIV PV+ cells from Tg(*Nkx2.1-Cre*):*RCE$^{f/f}$*:*Syngap1$^{f/+}$* mice. (**a**) Representative examples of individual eAMPA (negative deflections) and eNMDA (positive deflections) (5-10 pale sweep) and average traces (bold trace) recorded in PV cells from control (blue, n=16 cells, 7 mice) and cHet mice (red, n=14 cells, 7 mice). (**b, left**) Summary plots showing no change in the failure rate of eAMPA (left, LMM, p=0.550) and a significant decrease in the minimal (including failures and successes) eAMPA amplitude (**b, right** LMM, *p=0.031) and (**c**, left) charge transfer (LMM, *p=0.033) in cHet mice. (**c**, right) Summary bar graph illustrating the percentage of PV+ cells containing eNMDA in the thalamocortical evoked EPSC. (**d**) Synaptic latency histograms (bottom) of thalamocortical eEPSC from control and cHet mice, and summary bar graph (top) illustrating an increase in the onset

latencies of eEPSC in cHet mice (LMM, *p=0.023). For both histograms, bins are 0.1 msec wide. (**e**) Summary plots showing a significant decrease in the potency of eAMPA (successes only, LMM, **p=0.003, left) in cHet mice with no change in eNMDA (LMM, p=0.969), A significant increase is present in the NMDA/AMPA ratio (i.e. ratio of the peak for eNMDA and eAMPA, LMM, **p=0.001, right) in cHet mice. (**f**) Summary plots showing no significant differences in the eAMPA (LMM, p=0.177 for rise time, and p=0.608 for decay time) and eNMDA kinetics (LMM, p=0.228 for rise time, and p=0.221 for decay time). (**g**) Representative examples of individual LIV evoked EPSC (10 pale sweeps) and average traces (bold trace) with an interval of 50 ms recorded in two BC cells from control (blue) and cHet mice (red). (**h**) Summary plot showing significantly increased PPRs recorded from LIV BC cHet (red circles, n=8 cells; 5 mice) compared to controls (blue circles, n=9 cells, 5 mice), when two EPSCs were evoked in layer IV BC with two electric pulses at 30 or 50ms intervals (Two-way Repeated Measure ANOVA with Sidak's multiple comparison *post hoc* test, **p=0.001). * indicates p value <0.05; ** indicate p value <0.005.

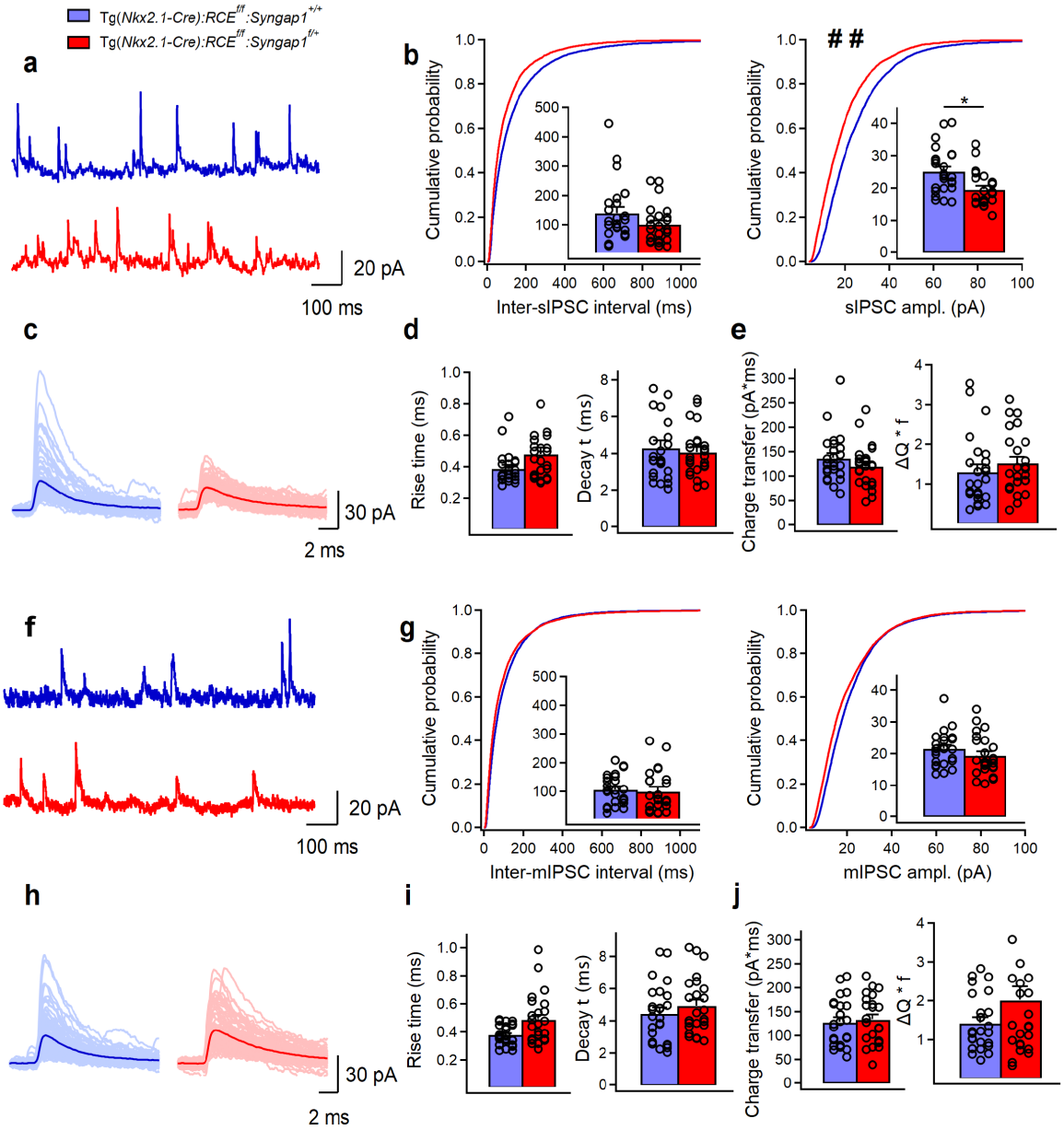

Figure 3. The amplitude of sIPSCs, but not mIPSCs, in LIV PV+ cells is reduced in Tg(*Nkx2.1-Cre*):*RCE$^{f/f}$*:*Syngap1$^{f/+}$* mice (**a**) Representative traces of sIPSCs recorded in PV+ cells from control (blue, n=25 cells, 8 mice) and cHet (red, n=24 cells, 7 mice) mice. (**b**) Cumulative probability plots show a significant decrease in the amplitude of sIPSC in cHet mice compared to control (LMM, ## p=0.003) and no change in the inter-sIPSC interval (LMM, p=0.106). Insets illustrate significant differences in the sIPSC amplitude for inter-cell mean comparison (LMM, *p=0.009) and no difference for inter-sIPSC interval (LMM, p=0.185). (**c**) Representative examples of individual sIPSC events (100 pale sweeps) and average traces (bold trace) detected in PV cells of

control and cHet mice. (**d**) Summary bar graphs for a group of cells show no significant differences in the sIPSCs kinetics (LMM, p=0.113 for rise time, and p=0.602 for decay time). (**e**) Summary bar graphs showing no differences for inter-cell mean charge transfer (LMM, p=0.234, left) and for the charge transfer when frequency of events is considered (LMM, p=0.273). (**f**) Representative traces of mIPSCs recorded in PV+ cells from control (blue, n=25 cells, 8 mice) and cHet (red, n=24 cells, 7 mice) mice. (**g**) Cumulative probability plots show no change in the amplitude of mIPSC (LMM, p=0.118) and in the inter-mIPSC interval (LMM, p=0.411). Insets illustrate summary data showing no significant differences in the amplitude (LMM, p=0.195) and the inter-mIPSCs interval for inter-cell mean comparison (LMM, p=0.243). (**h**) Representative examples of individual mIPSC events (100 pale sweeps) and average traces (bold trace) detected in PV+ cells of control and cHet mice. (**i**) Summary bar graphs for a group of cells show no significant differences in the mIPSCs kinetics (LMM, p=0.103 for rise time, and p=0.597 for decay time). (**j**) Summary bar graphs showing no differences for inter-cell mean charge transfer (LMM, p=0.374, left) and for the charge transfer when frequency of events is considered (LMM, p=0.100). * indicates p value <0.05 for bar graphs. # # indicates p value <0.005 for cumulative distribution.

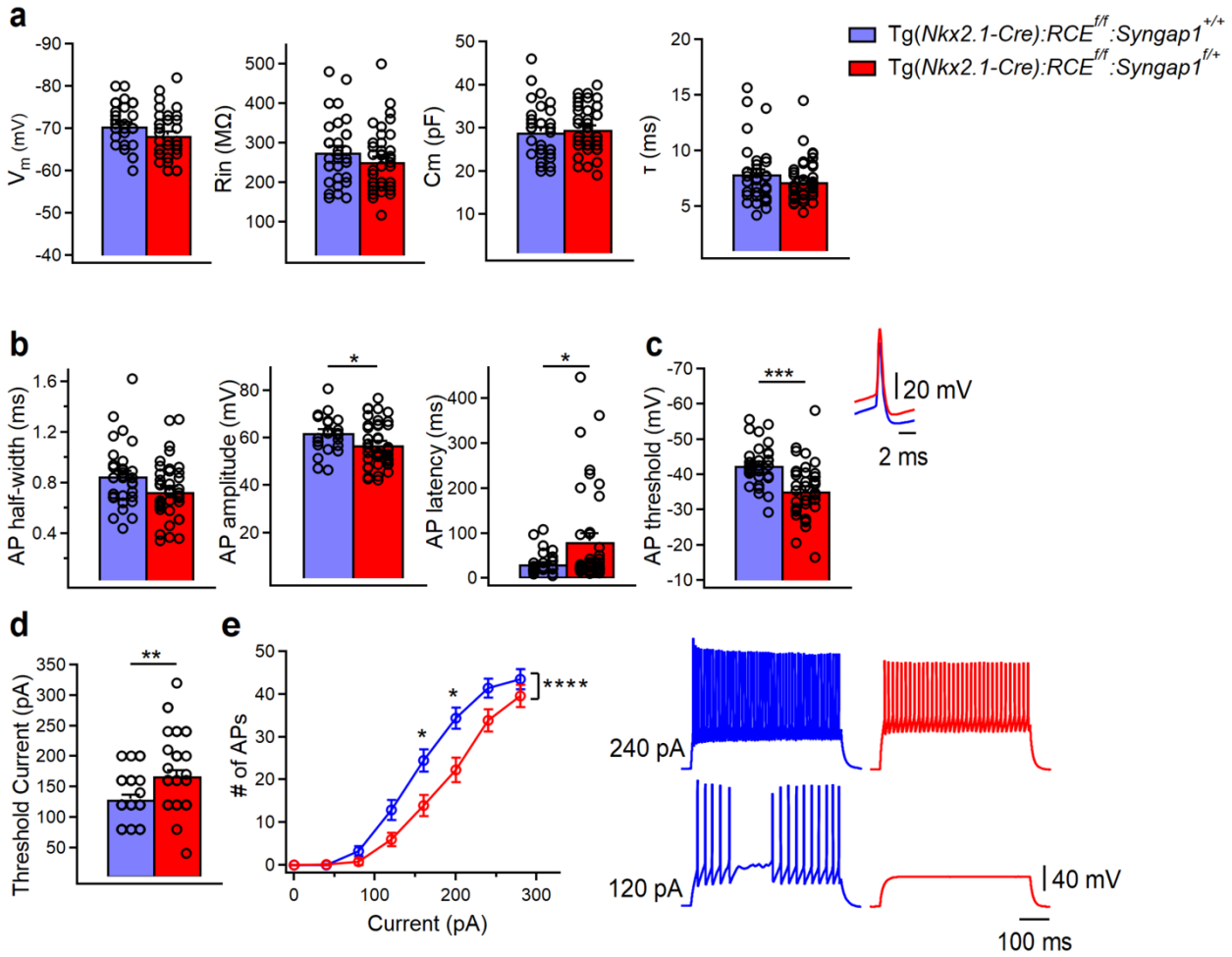

Figure 4. PV+ cells intrinsic excitability is decreased in Tg(*Nkx2.1-Cre*):*RCE*$^{f/f}$:*Syngap1*$^{f/+}$ mice. (**a**) Summary data showing no changes in the passive membrane properties between control (blue, n=33 cells, 15 mice) and cHet mice (red, n=40 cells, 17 mice) (LMM, p=0.081 for Vm, p=0.188 for Rin, p=0.188 for Cm, p=0.199 for τ). (**b**) Summary data showing no differences in AP half-width (LMM, p=0.111) but a significant decrease in AP amplitude (LMM, *p=0.032) and a significant increase in AP latency (LMM, *p=0.009) from PV+ cells recorded in cHet mice. (**c**, left) Summary bar graph shows a significant increase in AP threshold from cHet mice (LMM, ***p<0.001) for the first AP generated. (**c**, right top) Representative single APs evoked by threshold currents from control and cHet mice. APs are aligned at 50% of the rising phase on X axis and peak

on Y axis. Note the more hyperpolarized AP with consequent reduction in AP amplitude in PV+ cells from cHet mice. (**d**) Summary bar graph shows a significant increase in the threshold current (LMM, **p=0.004). (**e**, left) Summary plot showing a reduction of averaging number of APs per current step (40 pA) amplitude recorded from LIV PV+ cHet (red circles, n=38 cells; 18 mice) compared to control (blue circles, n=30 cells, 15 mice) neurons (Two-way Repeated Measure ANOVA with Sidak's multiple comparison *post hoc* test, ****p<0.0001). (**e**, right) Representative voltage responses indicating the typical FS firing pattern of PV+ cells in control and cHet mice in response to depolarizing (+120 pA and +240 pA) current injections corresponding to threshold current and 2x threshold current. * indicates p value <0.05; *** indicates p value <0.001; **** indicates value p<0.0001.

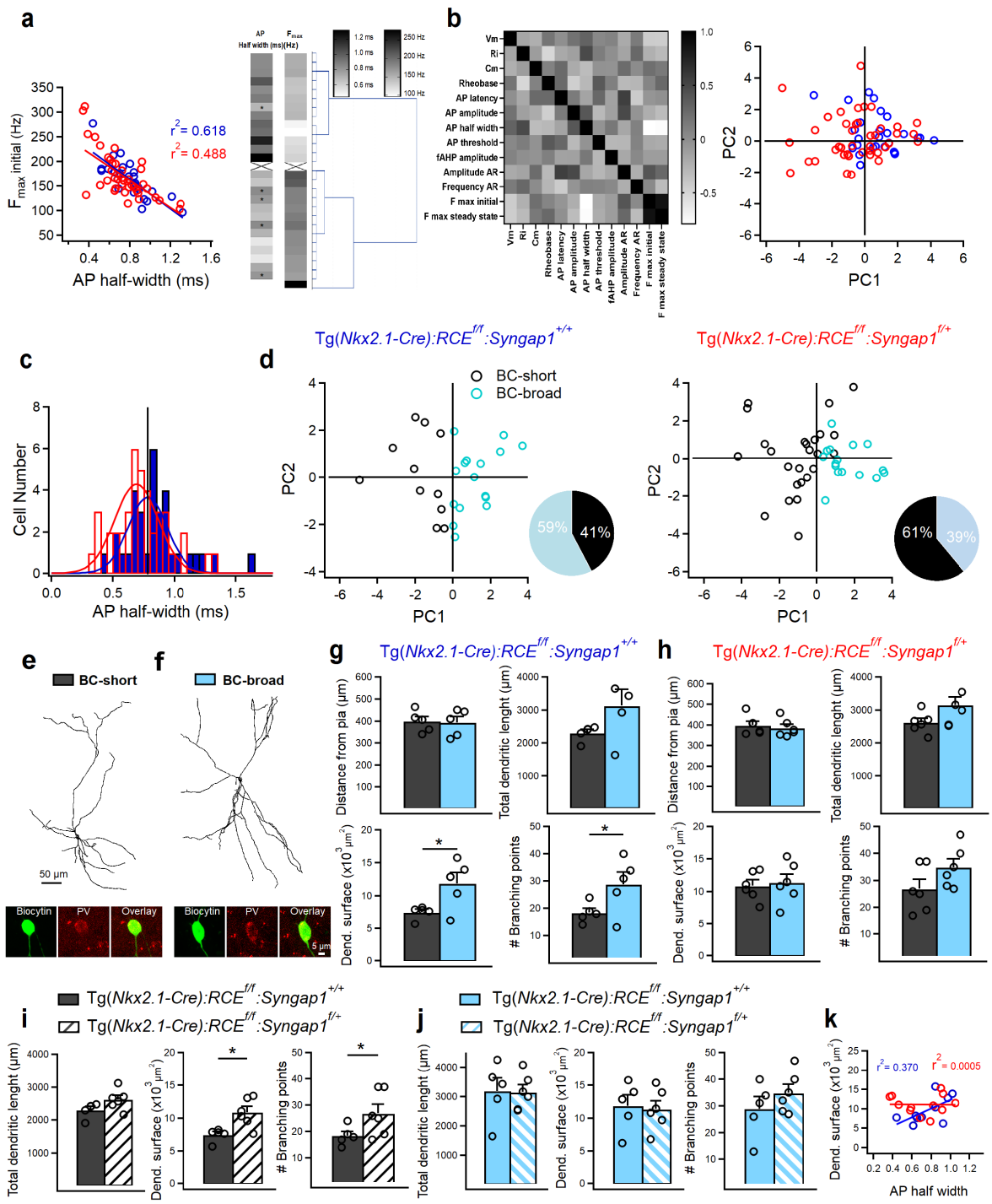

Figure 5. *Syngap1* haploinsufficiency in Nkx2.1+ interneurons affects the denritic arbour of a specific subpopulation of LIV PV+ cells. (**a**, left) Strong negative correlation of F_{max}initial with AP half-width in PV+ cells from control (blue, n=33 cells, 15 mice) and cHet mice (red, n=40 cells, 17 mice). (**a**, right) Hierarchical clustering based on Euclidean distance of PV+ cells from control mice. Clustering is based on AP half-width and Max frequency. Asterisks indicate cells with longer

AP half-width felling into the cluster including PV+ cells with higher of values of F_{max}initial. (**b**, left) Correlation of parameters describing membrane properties of PV+ interneurons. The 13 passive and active membrane properties used for PCA analysis (derived from 27 PV+ cells from control mice; see materials and methods) are arrayed against each other in a correlation matrix with the degree of correlation indicated by the shading: white is negatively correlated (correlation index of 0) ,black is positively correlated (correlation index of 1, diagonal squares) and light gray not correlated (correlation index of 0). PCA on the 13 parameters to reduce the dimensionality. (**b**, right) The first (PC1) and second (PC2) PC values derived for each interneuron are plotted against each other. No clear separation of subgroups in scatterplot of first 2 PCs is present when genotype is taken into consideration. (**c**) Cumulative histograms of AP half-widths in control (n=33 cells, 15 mice) and cHet mice (n=40 cells, 17 mice) fitted with two Gaussian curves. Vertical line indicates the cutoff value at intersection between the two curves. For both histograms, bins are 0.05 msec wide. (**d**) PCA analysis using the cutoff value of 0.78 ms and the 13 passive and active membrane properties distinguish two subgroups of PV+ cells with short (black circles) and broad (turquoise circles) AP-half width duration in both genotypes. Insets illustrate pie charts describing the % of two subgroups of PV+ cells in the control and cHet mice. (**e**) Anatomical reconstructions of a BC-short and (**f**) a BC-broad filled with biocytin in control mice during whole-cell patch-clamp recordings and post hoc immunohistochemical validation for PV. (**g**) Summary data in control mice (gray, BC-short n=5 cells, 4 mice; turquoise, BC-broad n=5 cells, 4 mice) showing no significant difference in terms of distance from pia (p=0.856, LMM) for both subtypes of PV+ cell analyzed indicating LIV location and significant differences in dendritic parameters between the two subpopulations of PV+ cells (LMM , *p= 0.016 for dendr. surface area, *p=0.043 for # branching points) and no change in total dendritic length (LMM , p=0.057). (**h**) Summary data in cHet mice (gray, BC-short n=6 cells, 4 mice; turquoise, BC-broad n=6 cells, 3 mice) showing no significant difference in terms of distance from pia (LMM, p=0.594) for both subtypes of PV+ cell and all dendritic parameters (LMM, p= 0.062 for total dendritic length, p=0.731 for dendr. surface area,

p=0.081 for # branching points). (**i**) Summary data showing a significant increase in dendritic complexity between control (gray, n=5 cells, 4 mice) and cHet (white, n=6 cells, 4 mice) for the subpopulation of BC-short (LMM , *p=0.009 for dendr. surface area, *p=0.048 for # branching points) and no difference for the total dendritic length (LMM, p=0.070). (**j**) Summary data showing preserved dendritic parameters in cHet (turquoise filled with pattern, n=6 cells, 3 mice) Vs control (turquoise, n=5 cells, 4 mice) (LMM, p= 0.967 for total dendritic length, p=0.784 for dendr. surface area, p=0.290 for # branching points). (**k**) The strong positive correlation of dendritic surface area with AP half-width is present only in PV+ cells from control mice (blue, n=10 cells, 8 mice) and disappears in cHet mice (red, 12 cells, 7 mice). * indicates p value <0.05.

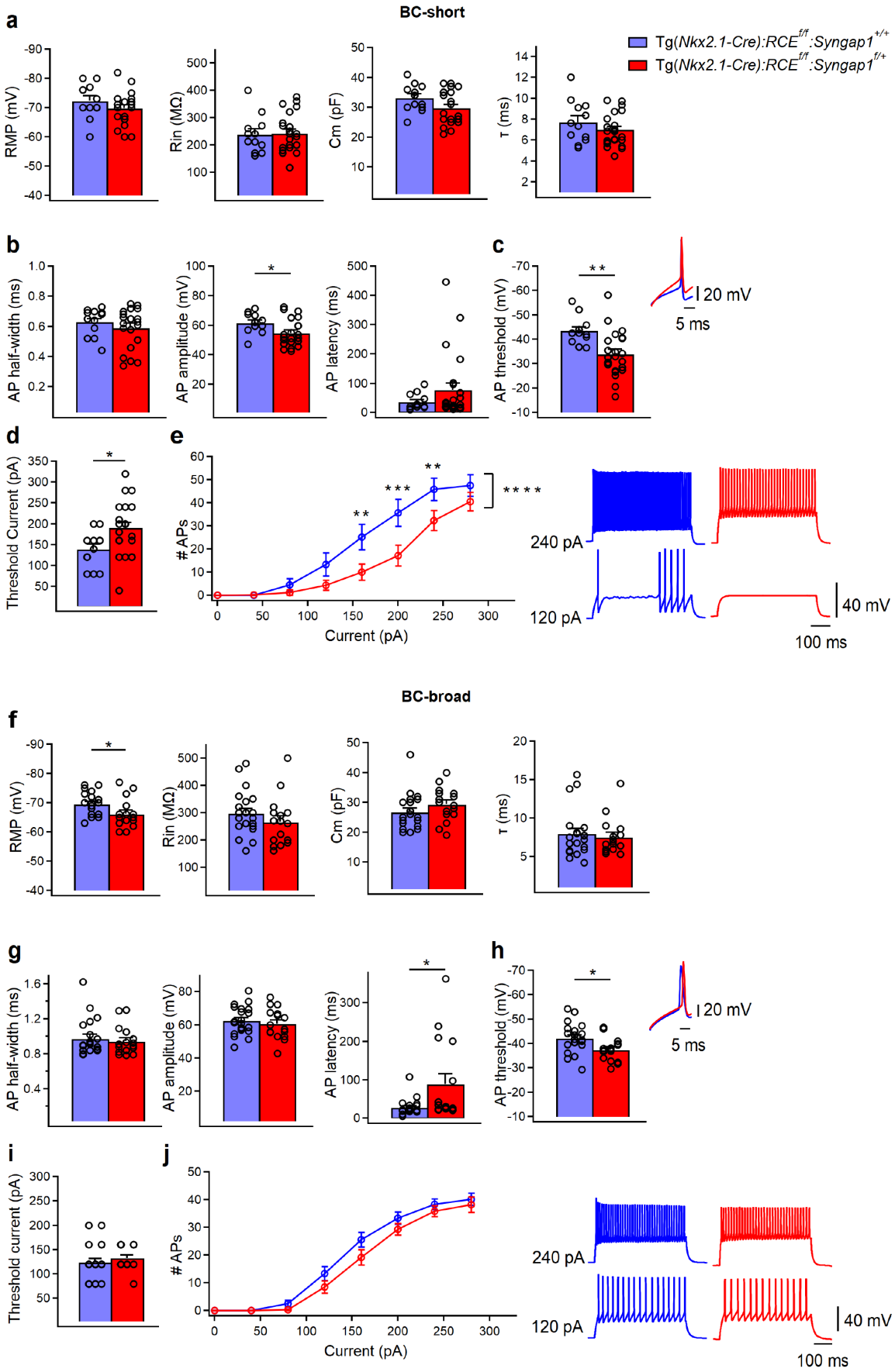
BC-short
Tg(Nkx2.1-Cre):RCE f/f:Syngap1 +/+
Tg(Nkx2.1-Cre):RCE f/f:Syngap1 f/+
RMP (mV)
Rin (MΩ)
Cm (pF)
τ (ms)
AP half-width (ms)
AP amplitude (mV)
AP latency (ms)
AP threshold (mV)
20 mV
5 ms
Threshold Current (pA)
APs
Current (pA)
240 pA
120 pA
40 mV
100 ms
BC-broad
Threshold current (pA)

Figure 6. Intrinsic excitability is decreased in both subpopulations of PV+ cells in cHet mice (**a**) Summary data showing no changes in the passive membrane properties of BC-short between control (blue, n=12 cells, 9 mice) and cHet mice (red, n=24 cells, 13 mice) (LMM , p=0.189 for Vm, p=0.856 for Rin, p=0.188 for Cm, p=0.077 for τ) (**b**) Summary data showing no differences in AP half-width (p=0.386, LMM) and AP latency (LMM, p=0.210) but a significant decrease in AP amplitude (LMM, *p=0.024) of BC-short recorded in cHet mice. (**c**, left) Summary bar graph shows a significant increase in AP threshold from cHet mice (LMM, **p=0.002). (**c**, right) Representative single APs evoked by threshold currents from control and cHet mice. (**d**) Summary bar graph shows a significant increase in the threshold current (LMM, *p=0.015). (**e**, left) Summary plot showing a reduction of averaging number of APs per current step (40 pA) amplitude recorded from LIV BC-short in cHet (red circles, n = 22 cells; 13 mice) compared to control (blue circles, n = 11 cells, 9 mice) neurons (Two-way Repeated Measure ANOVA with Sidak's multiple comparison *post hoc* test, **** p<0.0001). (**e**, right) Representative voltage responses indicating the typical FS firing pattern of BC-short in control and cHet mice in response to depolarizing (+120 pA and +240 pA) current injections corresponding to threshold current and 2x threshold current. (**f**) Summary data showing a significant decrease in RMP (LMM, *p=0.023) of BC-broad from cHet mice (red, n=16 cells, 11 mice) but no changes in the other passive membrane properties compared to control mice (blue, n=21 cells, 12 mice) (LMM, p=0.244 for Rin, p=0.170 for Cm, p=0.639 for τ). (**g**) Summary data showing no differences in AP half-width (LMM, p=0.593) and AP amplitude (LMM, p=0.713) and a significant increase in AP latency (LMM, *p=0.035) from BC-broad cells recorded in cHet mice. (**h**, left) Summary bar graph shows a significant increase in AP threshold from cHet mice (LMM, *p=0.010). (**h**, right) Representative single APs evoked by threshold currents from control and cHet mice. (**i**) Summary bar graph shows no difference in the threshold current (LMM, p=0.402). (**j**, left) Summary plot showing no difference in the averaging number of APs per current step (40 pA) amplitude recorded from LIV BC-broad in cHet (red circles, n=16 cells, 11 mice) compared to control (blue circles, n=18 cells; 11 mice) neurons (Two-way Repeated Measure

ANOVA with Sidak's multiple comparison *post hoc* test, p= 0.333). (**j**, right) Representative voltage responses indicating the typical FS firing pattern of BC broad in control and cHet mice in response to depolarizing (+120 pA and +240 pA) current injections corresponding to threshold current and 2x threshold current. * indicates p value <0.05; ** indicates p value <0.005.

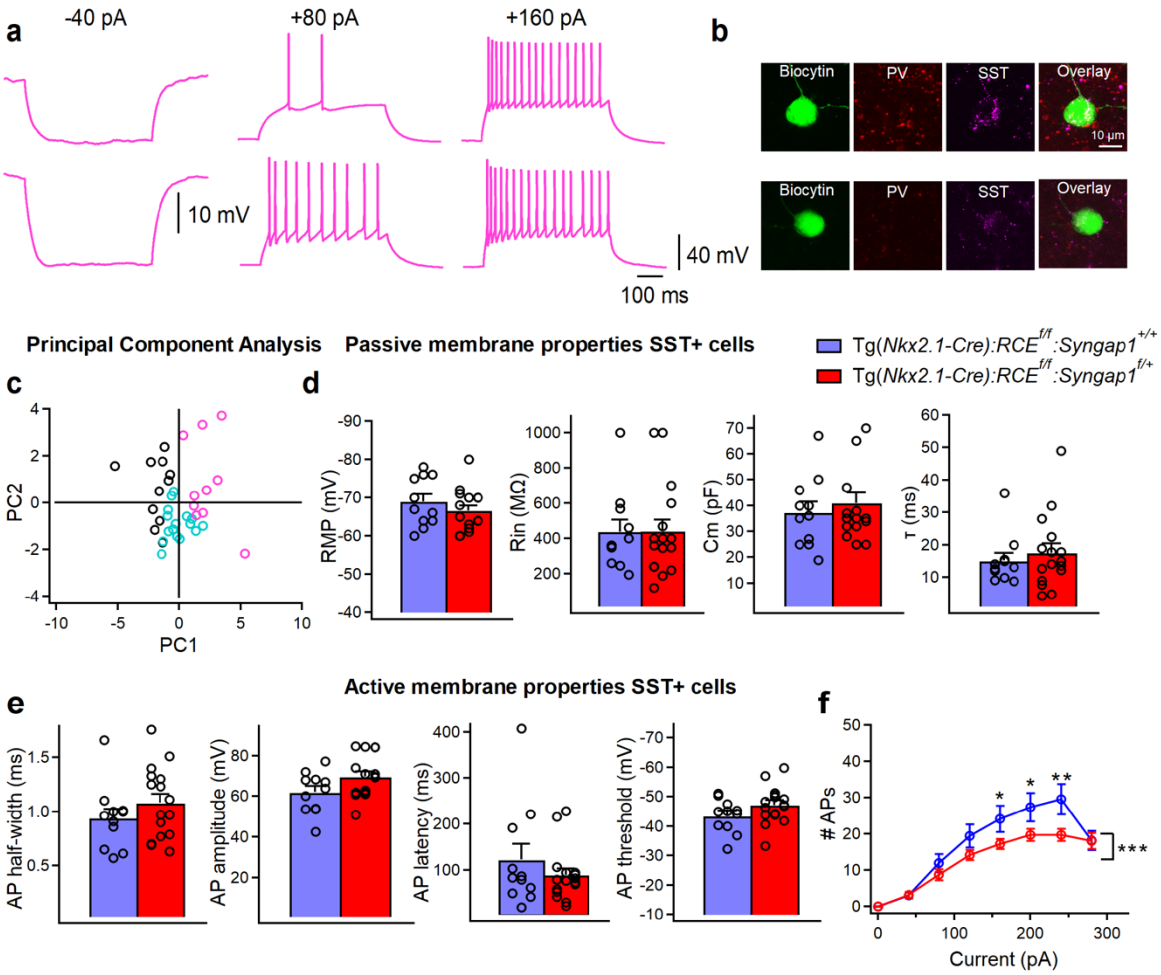

Figure 7. Evoked firing properties are reduced in SST+ cells from mice with embryonic-onset *Syngap1* haploinsufficiency in Nkx2.1 interneurons. (**a**) Representative voltage responses indicating the typical regular adapting firing pattern of SST+ in control mice in response to hyperpolarizing (-40 pA) and depolarizing (+80 pA and +160 pA) current injections corresponding to Ih associated voltage rectification, threshold current and 2x threshold current respectively. (**b**) Post hoc immunohistochemical validation of these interneurons confirming their positivity for SST+ and negativity for PV-. (**c**) PCA using the 13 parameters previously described clearly separate the cluster of SST+ cells (pink circles) from BC-short (black circles) having however some overlaps with BC-broad (turquoise circles) in control mice. (**d**) Summary data showing no changes in the passive (LMM, p=0.283 for Vm, p=0.959 for Rin, p=0.484 for Cm, p=0.501 for τ) and (**e**) active

membrane properties (LMM, p=0.332 for AP half-width, p=0.126 for AP amplitude, p=0.296 for AP latency, p=0.154 for AP threshold) between SST+ cells from control (blue, n=11 cells, 8 mice) and cHet mice (red, n=16 cells, 9 mice) (**f**) Summary plot showing a reduction of averaging number of APs per current step (40 pA) amplitude recorded from LIV SST+ in cHet (red circles, n= 16 cells, 9 mice) compared to control (blue circles, n=11 cells, 8 mice) neurons (Two-way Repeated Measure ANOVA with Sidak's multiple comparison *post hoc* test, ***p<0.001). * indicates p value <0.05; ** indicates p value <0.005.

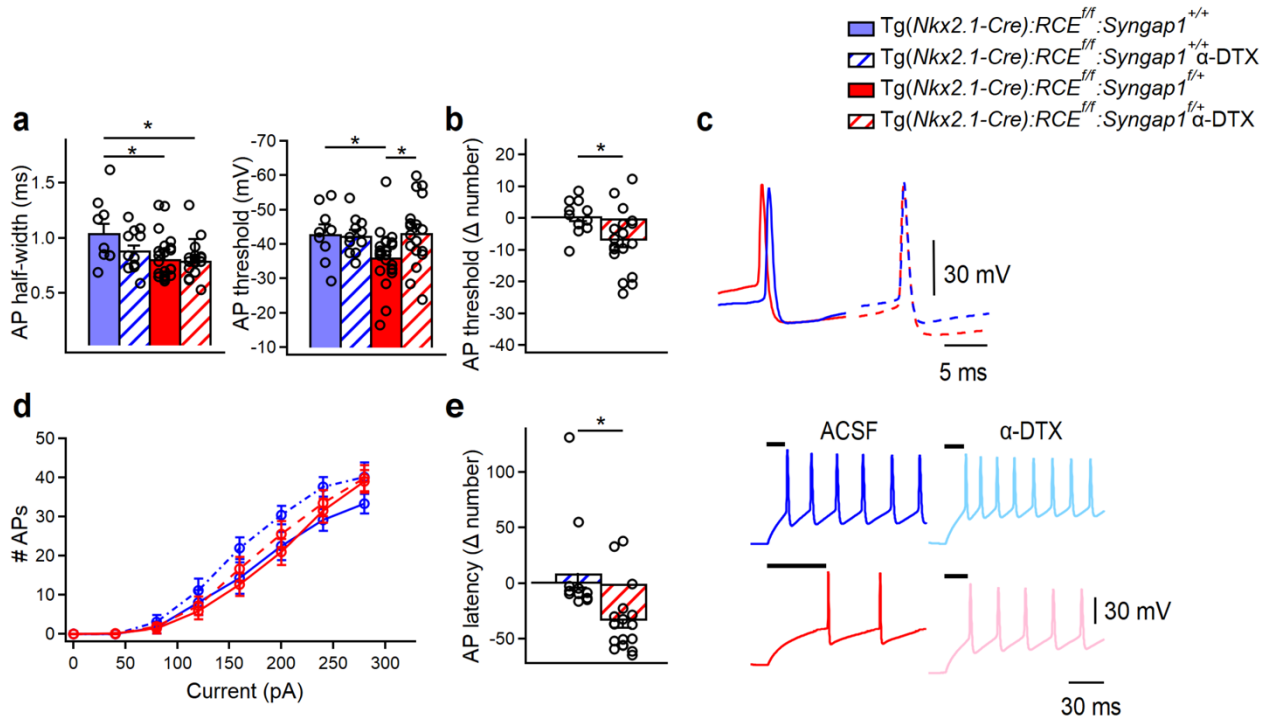

Figure 8. *Syngap1* haploinsufficiency alters the intrinsic excitability of LIV PV+ cells by affecting voltage-gated D-type K+ currents. (**a**, left) Summary bar graph shows a significant decrease in AP half-width in PV+ cells from cHet (red) vs control (blue) mice (LMM, *p=0.034), which persist when cHet PV+ cells are treated with α-DTX (red with diagonal stripes, LMM, *p=0.039). (**a**, right) Summary bar graph shows a significant increase in AP threshold of PV+ cells from vehicle-treated cHet mice (red) compared to vehicle-treated control mice (blue, LMM, *p=0.049) and the rescue of this deficit in presence of α-DTX (blue vs red with diagonal stripes, LMM, p=0.940). (**b**) Delta (Δ) value was calculated for AP threshold by subtracting individual values of α-DTX-treated cells from the average of their respective control group. A significant increase in AP threshold Δ number was found for cHet α-DTX-treated PV+ cells compared to control α-DTX-treated PV+ cells (LMM, *p=0.015). (**c**) Representative single APs evoked by threshold currents from vehicle-treated control (blue) and cHet (red) mice (center), and control (blue dotted line) and cHet α-DTX-treated (red dotted line) PV+ cells. (**d**) Summary plot showing no difference in the averaging number of APs per current step (40 pA) amplitude recorded from

LIV PV+ in cHet and control, both α-DTX-treated and vehicle-treated, PV+ cells (Two-way Repeated Measure ANOVA with Sidak's multiple comparison post hoc test, $p>0.05$). (**e**, left) Summary bar graph shows a significant difference in AP latency Δ number in α-DTX-treated cHet vs α-DTX-treated control PV+ cells (LMM, *$p=0.006$). (**e**, right) Representative voltage traces clearly show a reduction in the AP onset for cHet PV+ cells treated with α-DTX (pink trace) compared to vehicle-treated cHet PV+ cells (red trace), while control PV+ cells are not affected (vehicle treated-control PV+cells, blue traces; control α-DTX PV+ cells, light blue traces). Control mice: vehicle treated, n=9 cells from 4 mice; α-DTX-treated, n=11 cells from 6 mice; cHet mice: vehicle treated, n=23 cells from 10 mice; cHet α-DTX-treated, n=18 cells from 8 mice. * indicates p value <0.05.

Supplementary Figures

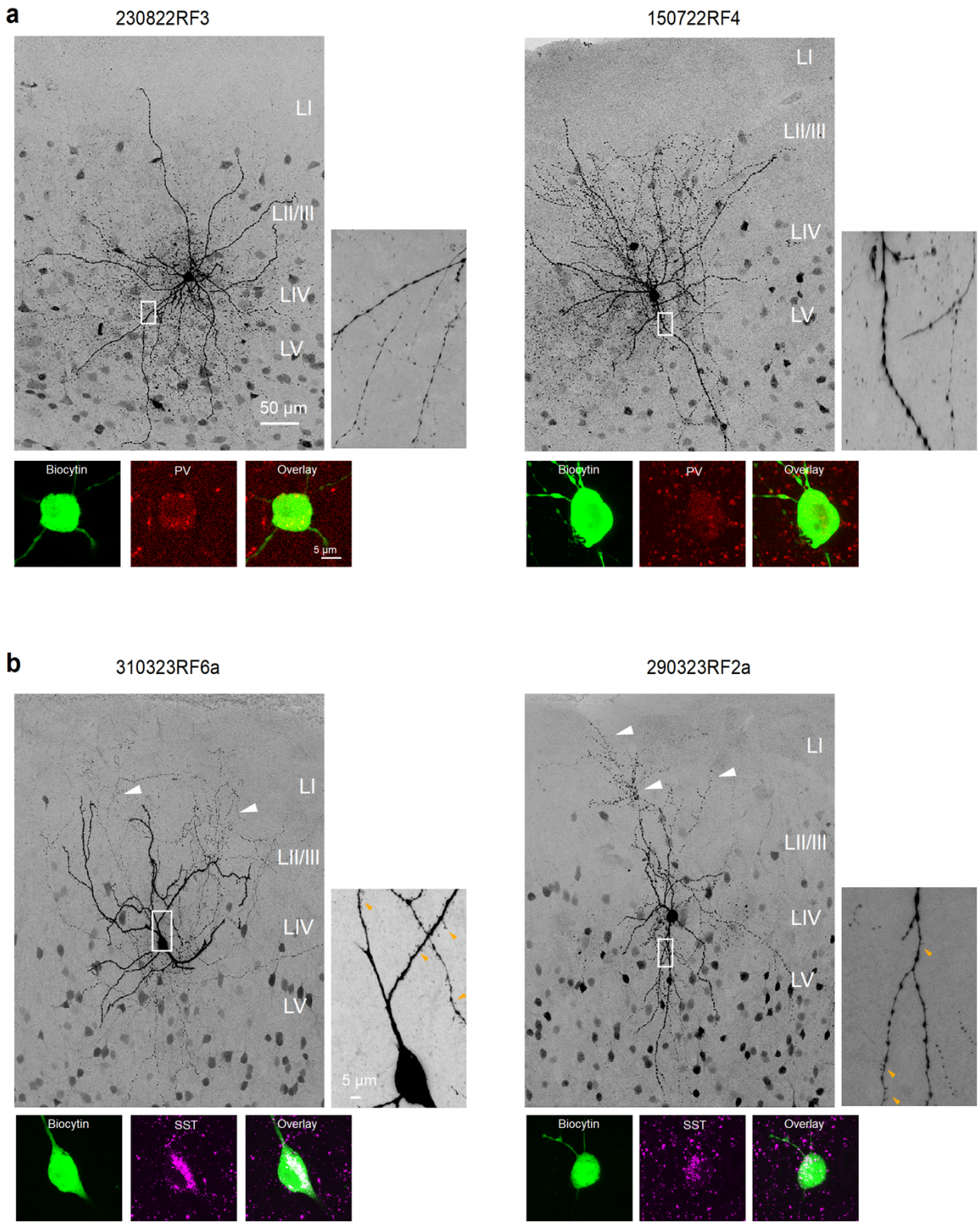

Supplementary Figure 1. Anatomical and neurochemical identification of LIV PV+ and SST+ interneurons in mouse primary auditory cortex. (**a, top**) Representative high-magnification

confocal images of two biocytin-filled PV+ cells with somata in LIV, showing multipolar dendritic arborization and smooth dendrites (small panels) and axons spreading from LII to LV. (**a, bottom**) Posthoc immunohistochemical validation showing immunopositivity for PV. (**b, top**) Representative high-magnification confocal image of two biocytin-filled typical SST+ cells with somata in LIV, showing multipolar (left) and bitufted (right) dendritic arborization characterized by the presence of spines (orange arrowheads, small panels), and axons projecting from LIV to LI where they give rise to multiple collaterals (white arrowheads). (**b, bottom**) Posthoc immunohistochemical validation showing immunopositivity for SST.

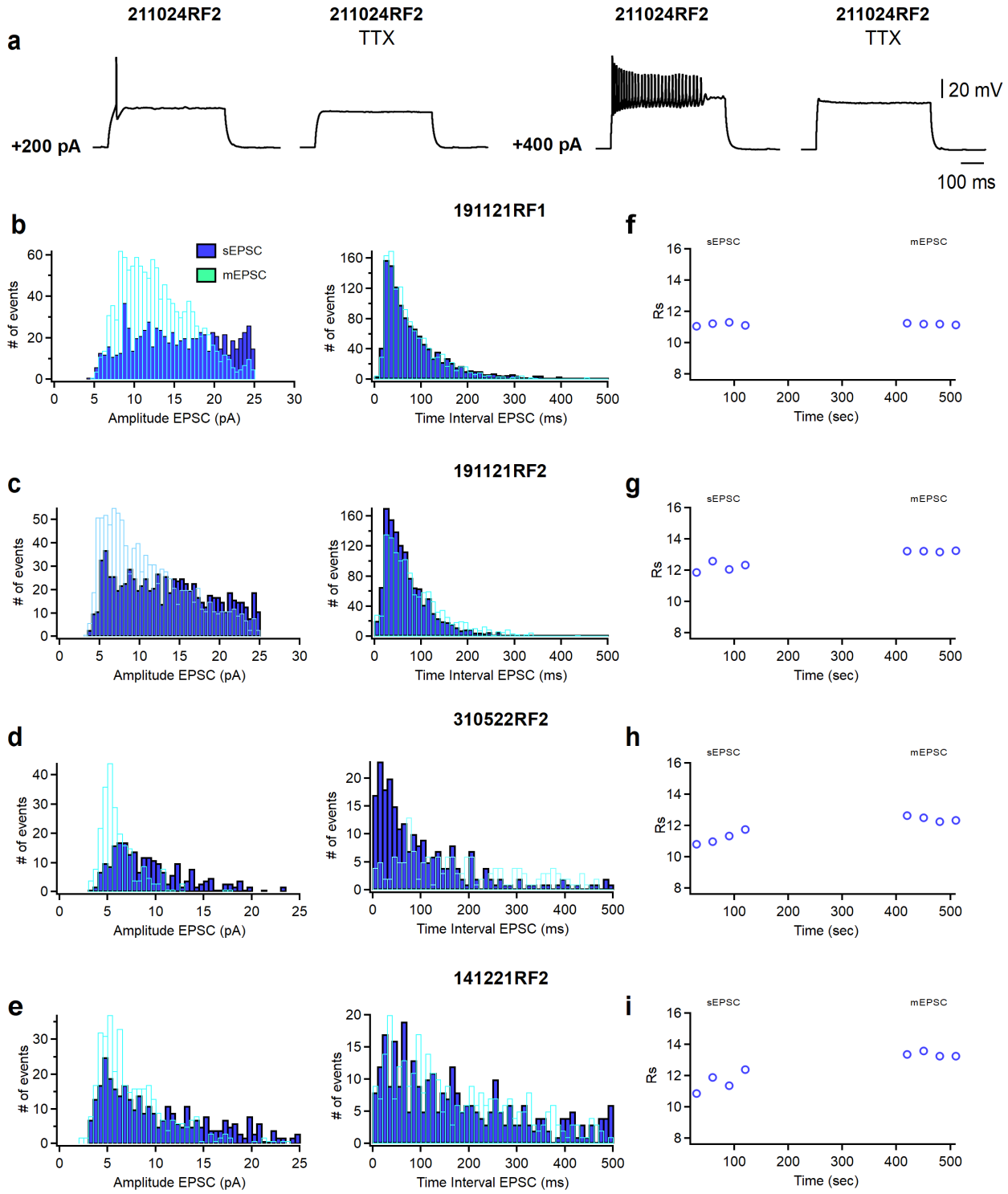

Supplementary Figure 2. Blockade of voltage-dependent Na+ channels by TTX abolished APs in PV+ cells from adult primary auditory cortex. (a) Representative voltage responses of a PV+ cell at threshold current (+200 pA) and 2x threshold current (+400 pA) in absence and presence of TTX. (**b-e**) Cumulative histograms of sEPSCs/mEPSCs amplitude (bin width 0.5 pA) and time

interval (bin width 10 ms) recorded from four PV+ cells. sEPSC were recorded for 2 minutes, then TTX (1μM; Alomone Labs) was perfused into the recording chamber. After 5 minutes, mEPSC were recorded for 2 minutes. (**f-i**) Time course plots of series resistance (Rs) of the four representative PV+ cells shown in **b-e** before (sEPSC) and during the application of TTX (mEPSC).

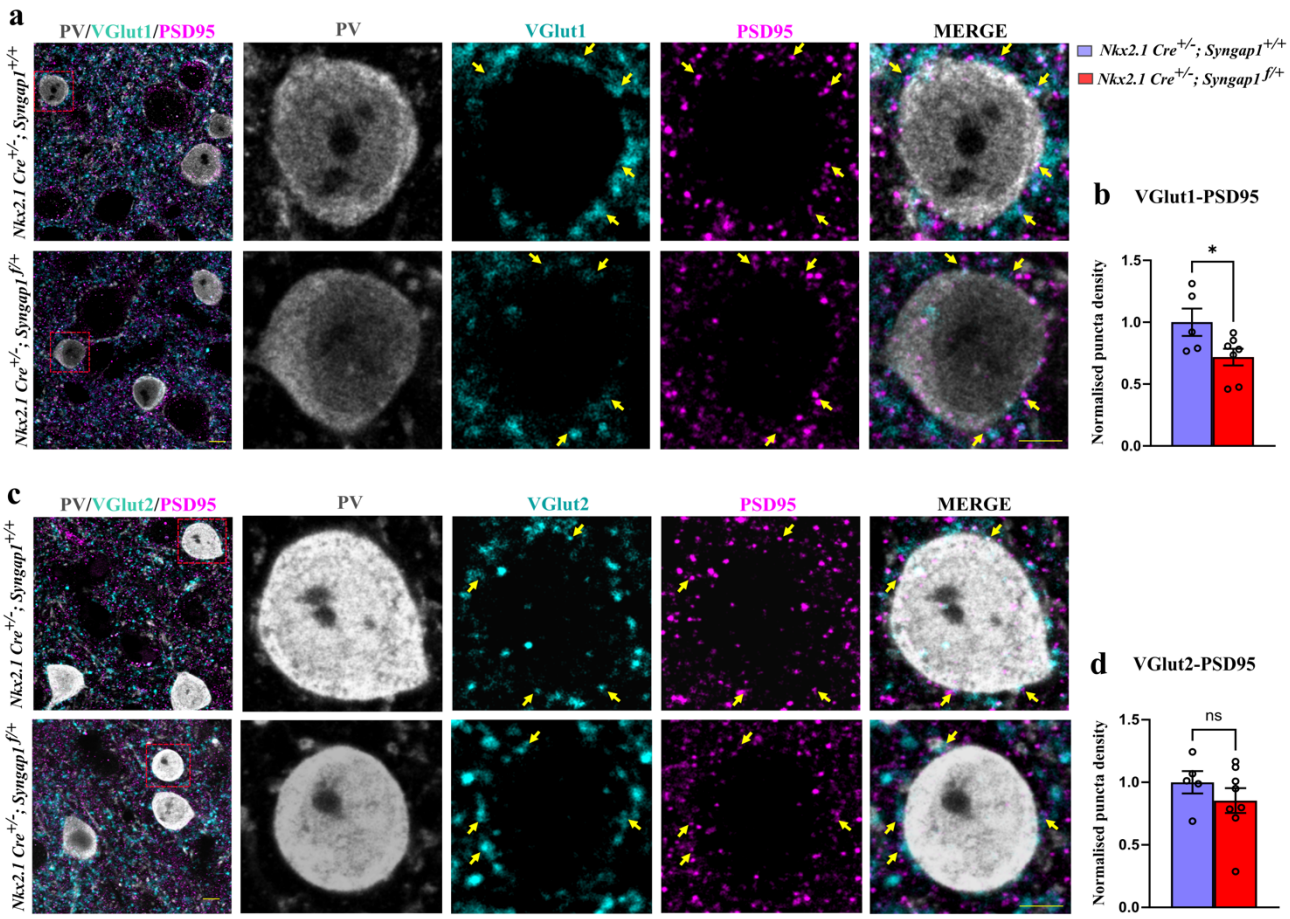

Supplementary Figure 3. *Syngap1* haploinsufficiency reduces the density of local vGlut1 excitatory inputs without affecting VGlut2 thalamocortical inputs to PV+ cell somata. (**a**) Representative images of auditory cortex immunolabelled for PV (grey), VGlut1 (cyan), PSD95 (magenta) in control (*Nkx2.1 Cre; Syngap1*$^{+/+}$) and cHet (*Nkx2.1 Cre; Syngap1*$^{flox/+}$) adult mice. Red squares indicate the location of cell bodies shown as high magnification images. Scale bar: 10 µm (**b**) Quantification of the density of perisomatic puncta colocalizing both VGlut1 and PSD95 normalised to controls (Unpaired t-test, *p= 0.0447). Number of mice: n=5 mice for control and n=7 for cHet. (**c**) Representative images of auditory cortex immunolabelled for PV (grey), VGlut2 (cyan), PSD95 (magenta). Scale bar: 10 µm (**d**) Quantification of of the density of perisomatic puncta colocalizing both VGlut2 and PSD95 normalised to controls (Unpaired t-test, p= 0.3345).

Number of mice: n=5 mice for control and n=8 for cHet. Yellow arrows indicate PV cell somata. Bar graphs represent mean ± SEM. ns $p > 0.05$ ns, not significant, * indicates p value <0.05.

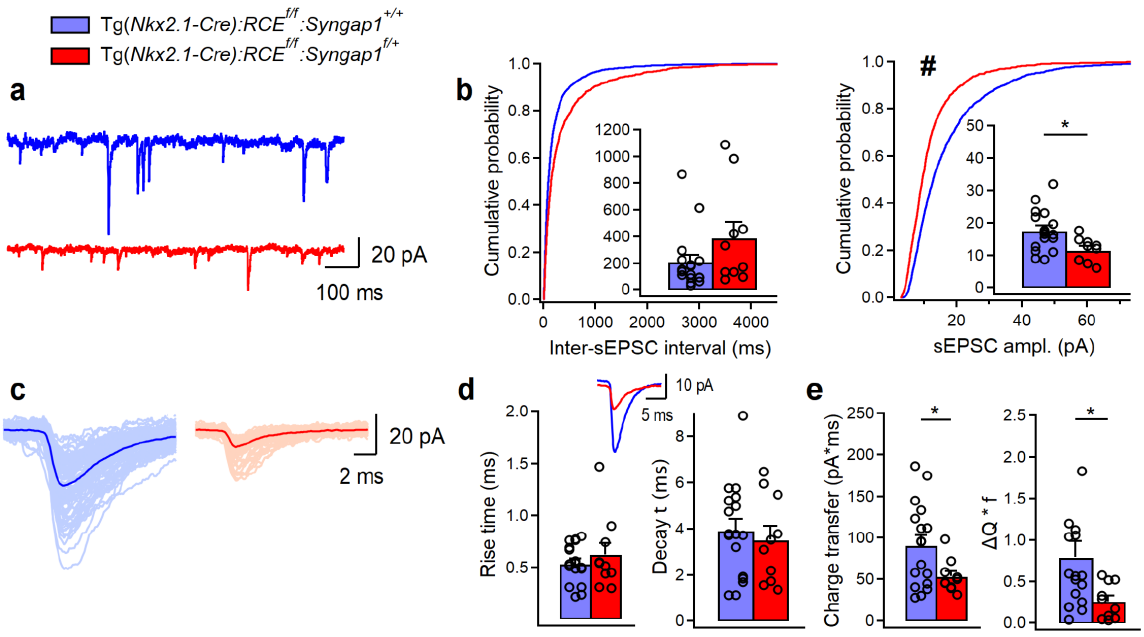

Supplementary Figure 4. sEPSC amplitude is reduced in LIV SST+ cells in Tg(*Nkx2.1-Cre):RCE$^{f/f}$:Syngap1$^{f/+}$* mice (a) Representative traces of sEPSCs recorded in SST+ cells from control (blue, n=17 cells, 10 mice) and cHet mice (red, n=10 cells, 8 mice). (b) Cumulative probability plots show a significant decrease in the amplitude (LMM, #p=0.010) and no change in the inter-sEPSC interval (LMM, p=0.126). Insets illustrate significant differences in the sEPSC amplitude for inter-cell mean comparison (LMM, *p=0.010) and no difference for inter-sEPSC interval (LMM, p=0.103. (c) Representative examples of individual sEPSC events (100 pale sweeps) and average traces (bold trace) detected in SST+ cells of control and cHet mice. (d) Superimposed scaled traces (left top) and summary bar graphs for a group of cells (bottom) show no significant differences in the sEPSCs kinetics (LMM, p=0.471 for rise time, and p=0.594 for decay time). (e) Summary bar graphs showing a significant decrease in cHet mice for inter-cell mean charge transfer (LMM, *p=0.047, left) and for the charge transfer when frequency of events is considered (LMM, *p=0.045). * and # indicates p value <0.05 for bar graph and cumulative distribution, respectively.

Supplementary data Francavilla et al., 2024

Results of statistical analysis performed with LMM for each data set

Yellow indicates significance

Table 1. sEPSCs and mEPSCs in LIV PV+ cells from control Vs cHet mice. Related to Fig. 1

	Control (n=14, 7 anim.)	**cHet (n=11, 6 anim.)**	**LMM**
sEPSC ampl.	17.92 ±1.32 pA	12.80±1.26 pA	F=7.067 p=0.014*
AUC sEPSC	63.02±11.92 pA x ms	34.54±2.96 pA x ms	F=3.135 p=0.090
sEPSC time interval	127.71±16.95 ms	253.21±77.99 ms	F=1.520 p=0.230
ΔQ * f	0.62±0.15	0.29±0.08	F=2.340 p=0.140
Rise time sEPSC	0.36±0.05 ms	0.30±0.03 ms	F=0.240 p=0.629
Decay time sEPSC	2.31±0.41 ms	1.62±0.18 ms	F=1.350 p=0.257
mEPSC ampl.	15.89±0.83 pA	13.34±1.58 pA	F=2.161 p=0.155
AUC mEPSC	64.51±10.25 pA x ms	30.51±2.52 pA x ms	F=7.506 p=0.012*
mEPSC time interval	99.42 ±11.62 ms	296.42 ±83.24 ms	F=4.049 p=0.056
Quantal content	1.14±0.07	1.01±0.07	F=1.824 p=0.189
ΔQ * f	0.73±0.12	0.18±0.03 ms	F=11.687 p=0.002**
Rise time mEPSC	0.41±0.07 ms	0.28±0.02 ms	F=1.285 p=0.269
Decay time mEPSC	2.91±0.66 ms	1.78±0.26 ms	F=1.779 p=0.193

Table 2. eAMPA and eNMDA currents in LIV PV+ cells from control Vs cHet mice. Related to Fig. 2

	Control (n=16, 7 anim.)	**cHet (n=14, 8 anim.)**	**LMM**
Failure rate (%)	7.75±2.95	10.57±3.89 pA	F=0.367 p=0.550
Minimal eAMPA	32.33±5.61 pA	17.67±2.51 pA	F=5.155 p=0.031*
AUC eAMPA	150.28±20.25 pA x ms	95.86±11.70 pA x ms	F=5.017 p=0.033*
Onset latencies eAMPA	4.27±0.11 ms (n=101, 7 anim.)	5.07±0.07 ms (n=114, 8 anim.)	F=5.261 p=0.023*
Rise time eAMPA	0.67±0.13 ms	0.90±0.09 ms (n=13, 7 anim.)	F=2.046 p=0.177
Decay time eAMPA	3.25±0.71 ms	3.71±0.49 ms (n=13, 7 anim.)	F=0.270 p=0.608
eNMDA	42.15±13.31 pA (n=6, 3 anim.)	41.73±7.57 pA (n=6, 5 anim.)	F=0.002 p=0.969
eAMPA in NMDA containing BC	50.51±9.98 pA (n=6, 3 anim.)	14.9±2.37 pA (n=6, 5 anim.)	F=14.455 p=0.003**
NMDA/ AMPA	0.88±0.28 (n=6, 3 anim.)	2.82±0.39 (n=6, 5 anim.)	F=18.876 p=0.001**
Rise time eNMDA	2.42±0.55 ms (n=6, 3 anim.)	3.90±0.85 ms (n=6, 5 anim.)	F=1.846 p=0.228
Decay time eNMDA	31.82±3.44 ms (n=6, 3 anim.)	63.33±21.22 ms (n=6, 5 anim.)	F=1.767 p=0.221

Table 3. sIPSCs and mIPSCs in LIV PV+ cells from control Vs cHet mice. Related to Fig. 3

	Control (n=25, 8 anim.)	**cHet (n=24, 7 anim.)**	**LMM**
sIPSC ampl.	25.15±1.39 pA	19.59±1.07 pA	F=5.229 p=0.009*
AUC sIPSC	136.83±9.71 pA x ms	120.42±8.74 pA x ms	F=0.976 p=0.385
sIPSC time interval	140.34±19.82 ms	101.61±13.01 ms	F=1.994 p=0.185
ΔQ * f sIPSC	1.31±0.17	1.53±0.15	F=0.538 p=0.587
sIPSC rise time	0.39±0.02 ms	0.48±0.04 ms	F=1.450 p=0.262
sIPSC decay time	4.31±0.39 ms	4.07±0.26 ms	F=0.1.88 p=0.831
mIPSC ampl.	21.55±1.08 pA	19.38±1.25 pA	F=1.726 p=0.195
AUC mIPSC	127.89±9.56 pA x ms	133.35±10.26 pA x ms	F=0.120 p=0.374
mIPSC time interval	106.44±10.43 ms	101.44±14.49 ms	F=0.115 p=0.739
Quantal content	1.19±0.05	1.06±0.05	F=3.077 p=0.086
ΔQ * f mIPSC	1.43±0.14	2.02±0.34	F=2.809 p=0.100
mIPSC rise time	0.38±0.01 ms	0.49±0.03 ms	F=2.907 p=0.103
mIPSC decay time	4.45±0.36 ms	4.94±0.35 ms	F=0.293 p=0.597

Table 4. Membrane properties of total LIV PV+ cells population in control Vs cHet mice. Related to Fig. 4

	PV cells in control (n=33) 15 animals	PV cells in cHet (n=40) 17 animals	LMM
Resting membrane potential (mV)	-70.51 ± 0.85	-68.32 ± 0.86	F=3.293 p=0.081
Input resistance (MΩ)	275.51 ± 14.15	251.02 ± 12.31	F=1.767 p=0.188
Membrane capacitance (pF)	29.00 ± 1.09	29.6 ± 0.87	F=1.767 p=0.188
Membrane time constant (ms)	7.88 ± 0.47	7.19 ± 0.30	F=1.679 p=0.199
Rheobase current (pA)	129.09 ± 6.69	167.00 ± 9.37	F=9.256 p=0.004**
AP threshold (mV)	-42.57 ± 1.01	-35.29 ± 1.22	F=17.519 p<0.001***
AP amplitude (mV)	62.06 ± 1.36	56.99 ± 1.49	F=5.079 p=0.032*
AP latency (ms)	31.44 ± 4.09	81.80 ± 17.00	F=7.136 p=0.009*
AP half width (ms)	0.85 ± 0.04	0.73 ± 0.03	F=2.697 p=0.111
AP rise time (10-90 % ms)	0.38 ± 0.01	0.34 ± 0.01	F=3.266 p=0.080
AP decay time (10-90 % ms)	0.73 ± 0.04	0.62 ± 0.03	F=2.628 p=0.115
fAHP (mV)	-15.50 ± 0.57	-16.96 ± 0.57	F=3.281 p=0.074
fAHP (ms)	3.41 ± 0.16	2.97 ± 0.13	F=2.840 p=0.103
I_h sag (mV)	0.75 ± 0.06	0.79 ± 0.10	F=0.100 p=0.752
SAAR	0.78 ± 0.01 (n=32)	0.74 ± 0.02	F=1.887 p=0.174
FFAR	1.35 ± 0.03 (n=32)	1.32 ± 0.02	F=0.473 p=0.496
Firing frequency at 2x rheobase current (Hz)	84.72 ± 4.98	101.6 ± 5.51	F=3.219 p=0.082
Fmax (Hz)	163.88 ± 7.32 (n=27)	171.84 ± 7.62	F=0.457 p=0.507
Fss (Hz)	102.33 ± 5.91 (n=27)	114.29 ± 5.68	F=1.421 p=0.243

Table 5.1. Morphological properties of BC-short Vs BC-broad in control mice. Related to Fig. 5.

	BC-short (n=5) 4 animals	BC-broad (n=5) 4 animals	LMM
Distance from pia (µm)	398.20 ± 21.40	392.40 ± 27.06	F=0.035 p=0.856
Soma perimeter (µm)	39.20 ± 2.16	40.68 ± 0.75	F=7.473 p=0.053
Number of dendrites	7.60 ± 0.67	7.60 ± 1.20	F=0.001 p=1.000
Number of branching points	18.40 ± 1.63	28.80 ± 4.55	F=5.778 p=0.043*
Number of terminals	28.60 ± 1.56	37.60 ± 6.26	F=2.427 p=0.158
Total dendritic lengt (µm)	2304.84 ± 103.86	3181.27 ± 440.23	F=4.933 p=0.057
Dendritic surface area (µm^2)	7483.76 ± 450.22	11859.68 ± 1653.16	F=9.263 p=0.016*

Table 5.2. Morphological properties of BC-short Vs BC-broad in cHet mice. Related to Fig. 5.

	BC-short (n=6) 5 animals	BC-broad (n=6) 3 animals	LMM
Distance from pia (µm)	398.33 ± 18.6	385.50 ± 17.48	F=0.302 p=0.594
Soma perimeter (µm)	41.40 ± 2.90	38.50 ± 0.66	F=1.143 p=0.310
Number of dendrites	5.00 ± 0.36	7.00 ± 0.68	F=7.998 p=0.032*
Number of branching points	26.83 ± 3.50	34.83 ± 3.11	F=3.493 p=0.081
Number of terminals	32.50 ± 3.61	42.33 ± 2.77	F=5.509 p=0.040*
Total dendritic lengt (µm)	2618.24 ± 128.54	3145.34 ± 243.28	F=4.403 p=0.062
Dendritic surface area (µm^2)	10864.15 ± 890.13	11358.15 ± 1248.32	F=0.125 p=0.731

Table 5.3. Morphological properties of BC-short in control Vs cHet mice. Related to Fig. 5.

	BC-short in control (n=5) 4 animals	BC-short in cHet (n=6) 4 animals	LMM
Distance from pia (µm)	398.20 ± 21.40	398.33 ± 18.64	F=0.001 p=0.996
Soma perimeter (µm)	39.20 ± 2.16	41.40 ± 2.90	F=0.488 p=0.523
Number of dendrites	7.60 ± 0.67	5.00 ± 0.36	F=15.364 p=0.002**
Number of branching points	18.40 ± 1.63	26.83 ± 3.50	F=5.294 p=0.048*
Number of terminals	28.60 ± 1.56	32.50 ± 3.61	F=1.190 p=0.305
Total dendritic lengt (µm)	2304.84 ± 103.86	2618.24 ± 128.54	F=4.640 p=0.070
Dendritic surface area (µm^2)	7483.76 ± 450.22	10864.15 ± 890.13	F=11.510 p=0.009*

Table 5.4. Morphological properties of BC-broad in control Vs cHet mice. Related to Fig. 5.

	BC-broad in control (n=5) 4 animals	BC-broad in cHet (n=6) 3 animals	LMM
Distance from pia (µm)	392.40 ± 27.06	385.50 ± 17.40	F=0.060 p=0.812
Soma perimeter (µm)	40.68 ± 0.75	38.50 ± 0.66	F=5.789 p=0.040*
Number of dendrites	7.60 ± 1.20	7.00 ± 0.68	F=0.205 p=0.662
Number of branching points	28.80 ± 4.55	34.83 ± 3.11	F=1.266 p=0.290
Number of terminals	37.60 ± 6.26	42.33 ± 2.77	F=0.541 p=0.481
Total dendritic lengt (µm)	3181.27 ± 440.23	3145.34 ± 243.28	F=0.002 p=0.967
Dendritic surface area (µm^2)	11859.68 ± 1653.16	11358.15 ± 1248.32	F=0.088 p=0.784

Table 6.1 Membrane properties of BC-short in control Vs cHet mice. Related to Fig. 6.

	BC-short in control (n=12) 9 animals	BC-short in cHet (n=24) 13 animals	LMM
Resting membrane potential (mV)	-72.33 ± 1.69	-69.79 ± 1.08	F=1.798 p=0.189
Input resistance (MΩ)	237.66 ± 19.98	242.00 ± 14.09	F=0.033 p=0.856
Membrane capacitance (pF)	33.08 ± 1.09	29.79 ± 0.87	F=3.331 p=0.077
Membrane time constant (ms)	7.75 ± 0.58	6.96 ± 0.31	F=1.818 p=0.187
Rheobase current (pA)	138.33 ± 12.42	190.00 ± 13.22	F=6.573 p=0.015*
AP threshold (mV)	-43.38 ± 1.63	-33.95 ± 1.84	F=11.458 p=0.002**
AP amplitude (mV)	61.43 ± 1.94	54.60 ± 1.86	F=5.570 p=0.024*
AP latency (ms)	36.36 ± 7.91	77.08 ± 22.70	F=1.631 p=0.210
AP half width (ms)	0.63 ± 0.02	0.59 ± 0.02	F=0.779 p=0.386
AP rise time (10-90 % ms)	0.31 ± 0.01	0.30 ± 0.01	F=0.146 p=0.705
AP decay time (10-90 % ms)	0.52 ± 0.02	0.49 ± 0.02	F=0.832 p=0.368
fAHP (mV)	-16.05 ± 1.06	-17.60 ± 0.77	F=1.423 p=0.241
fAHP (ms)	2.52 ± 0.10	2.50 ± 0.11	F=0.009 p=0.926
I_h sag (mV)	0.72 ± 0.12	0.80 ± 0.14	F=0.130 p=0.720
SAAR	0.81 ± 0.02	0.72 ± 0.03	F=3.715 p=0.062
FFAR	1.31 ± 0.06	1.33 ± 0.04	F=0.082 p=0.776
Firing frequency at 2x rheobase current (Hz)	100.83 ± 7.55	116.66 ± 7.24	F=1.977 p=0.169
Fmax (Hz)	191.97 ± 10.48 (n=11)	191.74 ± 10.14	F=0.001 p=0.989
Fss (Hz)	124.23 ± 9.32 (n=11)	131.72 ± 6.92	F=0.411 p=0.526

Table 6.2. Membrane properties of BC-broad in control Vs cHet mice. Related to Fig. 6.

	BC-broad in control (n=21) 12 animals	BC-broad in cHet (n=16) 11 animals	LMM
Resting membrane potential (mV)	-69.47 ± 0.87	-66.12 ± 1.25	F=5.895 p=0.023
Input resistance (MΩ)	297.14 ± 19.98	264.56 ± 22.55	F=1.405 p=0.244
Membrane capacitance (pF)	26.66 ± 1.30	29.31 ± 1.41	F=1.963 p=0.170
Membrane time constant (ms)	7.95 ± 0.67	7.52 ± 0.59	F=0.224 p=0.639
Rheobase current (pA)	123.80 ± 7.76	132.50 ± 6.02	F=0.731 p=0.402
AP threshold (mV)	-42.11 ± 1.31	-37.30 ± 1.18	F=7.313 p=0.010*
AP amplitude (mV)	62.42 ± 1.85	60.58 ± 2.28	F=0.140 p=0.713
AP latency (ms)	28.63 ± 4.63	88.86 ± 26.24	F=6.266 p=0.035*
AP half width (ms)	0.97 ± 0.04	0.94 ± 0.04	F=0.295 p=0.593
AP rise time (10-90 % ms)	0.43 ± 0.01	0.40 ± 0.01	F=1.513 p=0.232
AP decay time (10-90 % ms)	0.86 ± 0.04	0.82 ± 0.04	F=0.359 p=0.556
fAHP (mV)	-15.19 ± 0.67	-16.01 ± 0.79	F=0.620 p=0.440
fAHP (ms)	3.92 ± 0.16	3.67 ± 0.15	F=1.120 p=0.297
I_h sag (mV)	0.77 ± 0.07	0.78 ± 0.12	F=0.189 p=0.667
SAAR	0.75 ± 0.01	0.77 ± 0.02	F=1.715 p=0.202
FFAR	1.38 ± 0.03	1.32 ± 0.03	F=0.434 p=0.514
Firing frequency at 2x rheobase current (Hz)	75.52 ± 5.74 (n=20)	79.00 ± 4.50	F=0.984 p=0.331
Fmax (Hz)	144.58 ± 6.73 (n=16)	141.98 ± 6.50	F=0.746 p=0.396
Fss (Hz)	87.27 ± 5.04 (n=16)	88.14 ± 4.85	F=1.061 p=0.312

Table 7. Membrane properties of total SST+ cells population in control Vs cHet mice. Related to Fig. 7

	SST+ cells in control (n=11) 8 animals	SST+ cells in cHet (n=16) 9 animals	LMM
Resting membrane potential (mV)	-68.90 ± 1.92	-66.50 ± 1.35	F=1.203 p=0.283
Input resistance (MΩ)	436.45 ± 68.01	439.56 ± 65.91	F=0.003 p=0.959
Membrane capacitance (pF)	37.27 ± 1.09	40.87 ± 4.14	F=0.505 p=0.484
Membrane time constant (ms)	15.05 ± 2.31	17.42 ± 2.83	F=0.466 p=0.501
Rheobase current (pA)	61.81 ± 11.26	62.50 ± 8.73	F=0.003 p=0.960
AP threshold (mV)	-43.41 ± 1.71	-47.11± 1.57	F=2.165 p=0.154
AP amplitude (mV)	61.87 ± 3.05	69.57 ± 2.59	F=2.500 p=0.126
AP latency (ms)	121.98 ± 34.06	88.08 ± 14.36	F=1.141 p=0.296
AP half width (ms)	0.94 ± 0.09	1.08 ± 0.08	F=0.980 p=0.332
fAHP (mV)	-13.13 ± 1.05	-11.58 ± 1.03	F=1.289 p=0.278
I_h sag ratio	1.44 ± 0.47	0.82 ± 0.08	F=1.557 p=0.229
SAAR	0.82 ± 0.02 (n=10, 7 animals)	0.75 ± 0.03 (n=15, 9 animals)	F=2.289 p=0.144
FFAR	2.22 ± 0.52 (n=10, 7 animals)	3.12 ± 0.83 (n=15, 9 animals)	F=1.000 p=0.403
Firing frequency at 2x rheobase current (Hz)	36.60 ± 6.11 (n=10, 7 animals)	29.86 ± 1.67 (n=15, 9 animals)	F=1.719 p=0.203
Fmax (Hz)	125.09 ± 9.89 (n=10, 7 animals)	118.84 ± 10.02 (n=14, 8 animals)	F=0.061 p=0.808
Fss (Hz)	59.42 ± 6.37 (n=10, 7 animals)	47.58 ± 4.92 (n=14, 8 animals)	F=2.428 p=0.133

Table 8. Membrane properties of PV+ cells with and without α-DTX treatment in control and cHet conditions. Related to Fig. 8

	(1) PV+ cells in control (n=9) 4 animals	(2) PV+ cells in control + α-DTX (n=11) 6 animals	(3) PV+ cells in cHet (n=23) 10 animals	(4) PV+ cells in cHet + α-DTX (n=18) 8 animals	LMM 1 Vs 2	LMM 1 Vs 3	LMM 1 Vs 4	LMM 3 Vs 4
Resting membrane potential (mV)	-66.77 ± 0.95	-71.09 ± 2.02	-68.91 ± 1.22	-66.83 ± 1.48	p=0.143	p=0.293	p=0.973	p=0.320
Input resistance (MΩ)	281.11 ± 36.45	357.27 ± 63.01	274.13 ± 16.49	258.88 ± 20.92	p=0.313	p=0.837	p=0.560	p=0.555
Membrane capacitance (pF)	26.77 ± 2.05	27.18 ± 1.36	28.82 ± 1.19	29.27 ± 1.50	p=0.860	p=0.366	p=0.322	p=0.874
Membrane time constant (ms)	7.33 ± 1.00	9.34 ± 1.56	7.71 ± 0.44	7.48 ± 0.63	p=0.500	p=0.400	p=0.602	p=0.329
Rheobase current (pA)	142.22 ± 16.48	123.63 ± 10.02	166.95 ± 13.22	144.44 ± 12.99	p=0.520	p=0.308	p=0.833	p=0.263
AP threshold (mV)	-42.97 ± 2.68	-42.50 ± 1.60	-36.22 ± 1.67	-43.27 ± 2.30	p=0.871	*p=0.049	p=0.940	*p=0.022
AP amplitude (mV)	63.38 ± 2.54	64.10 ± 2.25	60.77 ± 1.75	61.89 ± 2.03	p=0.856	p=0.457	p=0.690	p=0.672
AP latency (ms)	45.72 ± 11.66	54.87 ± 13.57	89.96 ± 21.41	56.67 ± 7.03	p=0.606	p=0.686	p=0.329	p=0.093
AP half-width (ms)	1.05 ± 0.09	0.89 ± 0.05	0.81 ± 0.04	0.80 ± 0.03	p=0.114	*p=0.032	*p=0.039	p=0.783
fAHP (mV)	-15.07 ± 1.10	-14.41 ± 0.98	-16.66 ± 0.69	-12.28 ± 0.80	p=0.871	p=0.220	*p=0.046	***p<0.001
I_h sag (mV)	0.93 ± 0.14	0.68 ± 0.12	0.56 ± 0.07	0.63 ± 0.11	p=0.645	*p=0.047	p=0.118	p=0.575
SAAR	0.78 ± 0.02	0.82 ± 0.01	0.76 ± 0.02	0.82 ± 0.02	p=0.295	p=0.558	p=0.349	p=0.083
FFAR	1.32 ± 0.06	1.33 ± 0.06	1.27 ± 0.02	1.25 ± 0.03 (n=17)	p=0.886	p=0.344	p=0.279	p=0.572
Firing frequency at 2x rheobase current (Hz)	76.66 ± 9.07	80.90 ± 7.61	96.34 ± 6.13	86.77 ± 5.80	p=0.505	p=0.112	p=0.385	p=0.290
Fmax (Hz)	142.99 ± 10.14 (n=6)	160.34 ± 12.64	157.79± 6.41	175.29 ± 9.65 (n=16)	p=0.078	p=0.279	p=0.065	p=0.115
Fss (Hz)	91.16 ± 8.28 (n=6)	98.80 ± 10.91	106.37 ± 5.39	114.46 ± 6.33 (n=16)	p=0.178	p=0.220	p=0.057	p=0.327

Table S1. Membrane properties of BC-broad Vs BC-short in control mice. Related to Fig. 6

	BC-broad (n=21) 12 animals	BC-short (n=12) 9 animals	LMM
Resting membrane potential (mV)	-69.47 ± 0.87	-72.33 ± 1.69	F=2.511 p=0.126
Input resistance (MΩ)	297.14 ± 19.98	237.66 ± 19.98	F=4.830 p=0.036*
Membrane capacitance (pF)	26.66 ± 1.30	33.08 ± 1.09	F=10.973 p=0.02**
Membrane time constant (ms)	7.95 ± 0.67	7.75 ± 0.58	F=0.042 p=0.838
Rheobase current (pA)	123.80 ± 7.76	138.33 ± 12.42	F=1.020 p=0.323
AP threshold (mV)	-42.11 ± 1.31	-43.38 ± 1.63	F=0.373 p=0.546
AP amplitude (mV)	62.42 ± 1.85	61.43 ± 1.94	F=0.040 p=0.843
AP latency (ms)	28.63 ± 4.63	36.36 ± 7.91	F=0.871 p=0.358
fAHP (mV)	-15.19 ± 0.67	-16.05 ± 1.06	F=0.551 p=0.464
I_h sag (mV)	0.77 ± 0.07	0.72 ± 0.12	F=0.093 p=0.763
SAAR	0.75 ± 0.01	0.81 ± 0.02	F=3.644 p=0.066
FFAR	1.38 ± 0.03	1.31 ± 0.06	F=0.904 p=0.353
Firing frequency at 2x rheobase current (Hz)	75.52 ± 5.74 (n=20)	100.83 ± 7.55	F=7.082 p=0.012*
Fmax (Hz)	144.58 ± 6.73 (n=16)	191.97 ± 10.48 (n=11)	F=16.315 p<0.001***
Fss (Hz)	87.27 ± 5.04 (n=16)	124.23 ± 9.32 (n=11)	F=15.344 p<0.001***

Table S2. sEPSCs in SST+ cells from control Vs SST+ cells from cHet mice. Related to Fig. S4

	Control (n=17, 10 anim.)	**cHet (n=10, 8 anim.)**	**LMM**
sEPSC ampl.	17.63 ± 1.55 pA	11.63 ± 1.17 pA	F=7.850 p=0.010*
AUC sEPSC	90.75 ± 12.23 pA x ms	53.56 ± 6.05 pA x ms	F=4.942 p=0.047*
sEPSC time interval	209.07 ± 52.48 ms	390.24 ± 115.62 ms	F=2.858 p=0.103
ΔQ * f	0.79 ± 0.19	0.26 ± 0.06	F=4.438 p=0.045*
Rise time sEPSC	0.53 ± 0.04 ms	0.62 ± 0.11 ms	F=0.546 p=0.471
Decay time sEPSC	3.92 ± 0.49 ms	3.51 ± 0.59 ms	F=0.295 p=0.594